

ROTATIONAL WIDTHS FOR USE IN THE TULLY-FISHER RELATION. I. LONG-SLIT SPECTROSCOPIC DATA

BARBARA CATINELLA¹, MARTHA P. HAYNES², & RICCARDO GIOVANELLI²

Accepted for publication by the Astronomical Journal

ABSTRACT

We present new long-slit H α spectroscopy for 403 non-interacting spiral galaxies, obtained at the Palomar Observatory 5 m Hale telescope, which is used to derive well-sampled optical rotation curves. Because many of the galaxies show optical emission features which are significantly extended along the spectrograph slit, a technique was devised to separate and subtract the night sky lines from the galaxy emission. We exploit a functional fit to the rotation curve to identify its center of symmetry; this method minimizes the asymmetry in the final, folded rotation curve. We derive rotational widths using both velocity histograms and the *Polyex* model fit. The final rotational width is measured at a radius containing 83% of the total light as derived from I-band images. In addition to presenting the new data, we use a large sample of 742 galaxies for which both optical long-slit and radio HI line spectroscopy are available to investigate the relation between the HI content of the disks and the extent of their rotation curves. Our results show that the correlation between those quantities, which is well-established in the case of HI-poor galaxies in clusters, is present also in HI-normal objects: for a given optical size, star formation can be traced further out in the disks of galaxies with larger HI mass.

Subject headings: galaxies: kinematics and dynamics — galaxies: spiral — galaxies: structure — techniques: spectroscopic

1. INTRODUCTION

Accurately determined rotational velocities of spiral galaxies are important tools of extragalactic astronomy and cosmology. Among other applications, they serve to derive masses and redshift-independent distances of galaxies, to characterize the peculiar velocity field in the local universe, to probe the impact of tidal and collisional forces and to derive mass-to-light ratios and their evolution. Of particular note, the accuracy of the rotational velocity measurement is the single dominant contributor to the error budget of the Tully-Fisher (TF; Tully & Fisher 1977) relation, beyond the intrinsic scatter (Giovanelli et al. 1997b). The full characterization of a galaxy's velocity field ideally requires a two-dimensional map, such as can be obtained by means of HI synthesis, Fabry-Perot or fiber bundles. Such maps can provide direct evidence for departures in the velocity field from circular rotation and planarity and can best allow the extraction of the contribution of circular rotation. However, those techniques have become available relatively recently, and they are still observationally costly (Fabry-Perot systems do not allow for simultaneous sampling of the velocity channels) or characterized by limited spatial dynamic range (fiber bundles). For these reasons, the vast majority of velocity width data have relied on simpler, albeit cruder, observations, e.g. one-dimensional rotation curves (RC) $V(r)$ obtained with single-slit spectrographs placed along a spiral disk's

major axis or, even more commonly, with the zero-th order approach of 21cm global (i.e., spatially integrated) line profiles obtained with single radio dishes. In practical situations such as wide area peculiar velocity studies exploiting the TF relation, it is often necessary to combine rotational velocity measures obtained from multiple methods. In such cases, it is imperative to devise width measurement algorithms that are both robust and minimize technique-based bias or systematic effects. This paper is the first of a series in which we use a large compilation of both global HI line profiles and optical long-slit spectra to minimize such systematics for TF applications and to derive a statistical characterization of how disks rotate.

Most optical studies of rotation velocities in the low redshift universe concentrate on the red part of the optical spectrum, made attractive by the presence of several nebular lines, most prominently H α at 6563Å and [NII] $\lambda\lambda$ 6548,6584Å. The radial variation of the observed rotational velocities – the rotation curve – offers insight into the velocity field but must be interpreted in light of assumptions about dark matter components, spatial and kinematic disturbances and asymmetries, the impact of extinction, and likely biases induced by differences in the global star formation history. Several recent works have contributed significant compilations of velocity widths based on optical long-slit spectra, including Mathewson et al. (1992), Mathewson & Ford (1996), Courteau (1997, hereafter C97), Vogt (1995), Vogt et al. (2004a), Dale (1998), and Dale et al. (1997, 1998, 1999a,b,c, 2001). Rotational widths presented by those authors have been derived using several different algorithms, based either on velocity histograms (Mathewson, Vogt, and their collaborators) or on functional fits to the RCs (C97; Dale and collaborators). The current work presents new data and widths based on a measurement

¹ National Astronomy and Ionosphere Center, Arecibo Observatory, HC3 Box 53995, Arecibo, PR 00612, USA; bcatinel@naic.edu. The National Astronomy and Ionosphere Center is operated by Cornell University under a cooperative agreement with the National Science Foundation.

² Center for Radiophysics and Space Research and National Astronomy and Ionosphere Center, Cornell University, Ithaca, NY 14853, USA; haynes@astro.cornell.edu, riccardo@astro.cornell.edu.

technique belonging to the second category. Discussion of the systematics using a large compilation including all of the above referenced datasets but with rotational widths remeasured on the digital spectra according to the technique presented here will be presented separately (Catinella et al. 2005b, hereafter Paper II).

The principal issue is: given a RC, what specific measurement of a characteristic velocity width best reflects a physical quantity tied to the galaxy’s rotational velocity. The circular velocity field of a galaxy can be calculated from the expression describing the gravitational potential of the system, under the assumption of centrifugal equilibrium. In the case of an infinitely thin disk, characterized by an exponential surface density distribution with scale length r_d , it can be shown (Freeman 1970) that the resulting RC reaches a peak at $2.12 r_d$, and approaches the asymptotic Keplerian law at larger galactocentric distances. In this simple case, one could identify the velocity width with the value of the maximum rotation of the disk (or twice its value). The observational discovery that most RCs are not falling, but rather flat or even rising at the edge of the optical disk, raised the issue of accounting for matter that was not detectable except for its gravitational effects. The circular velocity field should be thus calculated from the sum in quadrature of two terms, related to the exponential disk and the dark matter halo; the effect of a stellar bulge can be included similarly.

For simplicity, the “dark” halo is usually assumed to be spherical. Two common choices for the expression of its radial density distribution are the so-called isothermal and NFW (Navarro et al. 1997) profiles, the latter derived from N-body simulations of structure formation in hierarchically clustering universes. The observed RCs, or at least their large-scale, smooth behavior (neglecting spiral streaming, bar perturbations, disk warps or asymmetries, and so on), can be successfully modeled using these components, and giving them appropriate weights in order to optimize the results. The presence of a dark matter halo complicates however the definition of rotational width, since it should no longer be associated with the peak of the RC, but the appropriate radial distance at which a characteristic width measurement should be made is not obvious. While several authors measure rotational velocities at $2.15 r_d$ (e.g., Chiba & Yoshi 1995 and C97), others prefer to do it at the optical radius R_{opt} , i.e., the radius encompassing 83% of the total integrated light of the galaxy (e.g., Persic et al. 1996; Giovanelli et al. 1997a. For comparison, $R_{\text{opt}}=3.2 r_d$ for an exponential disk). The sampling of the velocity fields at larger galactocentric distances offers important advantages in terms of smaller extinction and shallower (if not null) velocity gradient, since both dust fraction and RC slope decrease with increasing radius. For these and other reasons, further discussed here and in Paper II, we adopt R_{opt} as reference radius for width measurements. Our approach to determining rotational velocities from long-slit RCs is described in detail in this work. Rotational velocities obtained from optical long-slit spectra should, however, be compared to radio widths derived from HI integrated line profiles, using large samples of galaxies with both measurements available. This is a key element to address the issue of a reference scale for RC width measurements. Since HI emission can be traced out to radial distances

that are typically twice as large as those sampled by HI regions, HI widths should provide, in fact, more reliable estimates of the maximum rotation of the disks. Such comparison will be presented in Paper II.

This paper is organized as follows: We describe our sample selection criteria, observation strategy, and data reduction process in Section 2. The RC extraction and folding technique are discussed in Sections 3 and 4. We illustrate our velocity width measurement method in Section 5, and present our results in Section 6. The relation between the distributions of the H α and HI line emissions in the disks, which is relevant to the determination of velocity widths, is investigated for a large overlap sample with both radio and optical spectroscopy in Section 7, and our conclusions are summarized in Section 8.

2. OBSERVATIONS AND DATA REDUCTION

The optical long-slit spectroscopy presented in this work was obtained at the Palomar Observatory 5 m Hale³ telescope. A total of 20 nights (19 of which had weather conditions adequate for spectroscopy) were allocated over the course of five observing runs. To minimize overheads and maximize throughput, spectra were obtained using only the red camera of the Double Spectrograph (Oke & Gunn 1982) at the Cassegrain focus ($f/15.7$). The combination of the 1200 lines mm^{-1} grating and a $2''$ wide slit yielded a dispersion of $0.65 \text{ \AA pixel}^{-1}$; the spatial scale of the CCD was $0.468'' \text{ pixel}^{-1}$. The grating angle was set in order to obtain a spectral coverage of 6530-7180 \AA , allowing detection of the H α line up to $cz \simeq 28,000 \text{ km s}^{-1}$. In addition, a small number of spectra were acquired with similar instrumental setup during other observing runs by members of our group. A few galaxies have been observed more than once to check the consistency among different runs. Of the 532 galaxies targeted, 488 show H α emission (12 of the remaining ones show H α in absorption; the other 32 have continuum but no line emission within the observed wavelength range). The final number of galaxies with useful, extended RCs is 403.

The sample targeted for the long-slit observations was extracted from a larger set of spirals identified as good TF candidates for inclusion in a photometric I-band survey carried out by M.P.H., R.G., and collaborators as a part of an effort to map the peculiar velocity field in the local Universe. Several datasets containing I-band photometry, optical RCs derived from long-slit spectra, and global HI profiles all in digital format contribute to what will be referred to as the SFI++ sample; details of this compilation will be discussed more fully elsewhere (Catinella 2005; Masters et al., in preparation). The spectroscopic sample presented here includes undisturbed, inclined spirals with apparent diameter greater than $0.6'$, as estimated from a quick-look examination of the I-band images. The targets were identified principally to provide adequate TF target sampling in the sky area just south of the celestial equator, $-15^\circ \leq \delta \leq 0^\circ$, and to provide optical rotation widths for objects for which HI global profiles were not available for one of

³ The Hale telescope at the Palomar Observatory is operated by the California Institute of Technology (Caltech) under cooperative agreement with Cornell University and the Jet Propulsion Laboratory.

various reasons. The resulting sample for the $H\alpha$ spectroscopy was heterogeneous, and included three types of targets: (a) galaxies with no spectroscopy (optical or radio) available; (b) galaxies with problematic HI profiles (due to confusion within the radiotelescope beam, or with irregular, asymmetric profiles, where a velocity width could not be clearly determined), and (c) a minority of nearby galaxies with apparent sizes larger than the spectrograph slit, where observations obtained at multiple offset positions along the major axis were required to trace the full extent of the velocity field. A few additional targets (14 galaxies) for which I-band photometry was not available were observed to fill in gaps in our observing schedule.

Due to the heterogeneous composition of the observational sample, we adopted a slightly different observing strategy depending on the category (a, b, or c in the previous paragraph) to which each target belonged. In the absence of previously available spectroscopic information (the majority of the cases), we performed a first, 5 minute integration on the target. A quick inspection of the spectrum allowed us to check for the presence of extended galaxy line emission, and to estimate the strength of the spectral lines. If the observation was deemed useful for TF purposes, a second integration long enough to adequately sample the outer disk regions (typically 10-15 minutes) was performed. For some other targets, prior information on the strength of HI line emission suggested that $H\alpha$ would be detectable; in such cases, we performed a 10 minute integration. Finally, in those cases where the 128''-long slit did not sample the full extent of the RC, we acquired one or more “offset” spectra, displaced by multiples of 45'' from the central position, along the major axis of the galaxy. This technique was particularly designed to insure that the outer parts of large objects are adequately sampled.

The spectra have been reduced using standard and customized IRAF⁴ tasks. The standard reduction procedure includes the following steps: bias subtraction, flat-fielding, cosmic ray cleaning, line-curvature correction (modeled from the night sky emission lines; the “S-distortion” was found not to be significant and thus ignored), and wavelength calibration (using the sky lines). Multiple exposures of the same galaxy at the same slit position were co-added, sky lines and galactic continuum were fit with polynomials and then subtracted from the spectra. In the remainder of this section, we will discuss the sky subtraction in detail, focusing on the case of galaxies with line emission significantly extended relative to the size of the slit.

2.1. A New Technique for Sky Line Subtraction

The *standard* sky subtraction technique requires the identification of *signal-free* regions on both sides of the galaxy line emission, along the spatial direction; for each spectral channel, the sky lines in those narrow strips are then interpolated with a low-order (2 or 3, typically) polynomial, and subtracted from the spectrum. Such

a procedure is clearly not applicable if the galaxy line emission fills the spectrograph slit. In particular, this problem affects 73 galaxies in our sample which are sufficiently extended to require offset observations. We thus developed a modification of the standard technique to deal with this issue.

We illustrate our technique (which will be referred to as *template* sky subtraction) using the galaxy MCG-2-31-017 (AGC 520006) as an example. MCG-2-31-017 is an Scd spiral, characterized by weak continuum and strong line emission; its heliocentric velocity is 4460 km s⁻¹. Figure 1a shows the portion of its spectrum that includes the galaxy emission lines (before continuum and sky subtraction). The horizontal and vertical axes correspond to spatial position along the slit and dispersion, respectively. The $H\alpha$ line is the most prominent feature in the lower half of the spectrum. The lack of signal-free regions at the edges of the slit leads to a very poor sky line subtraction, when the standard procedure is applied (Figure 1c; the galaxy continuum emission has also been removed). The use of a few pixels on both sides of each row of Figure 1a cannot, in fact, constrain the shape of the sky and continuum emission, except at the very edges of the slit, and thus the sky subtraction leaves large residuals across the spectrum (horizontal chop in Figure 1c). The result for the sky line-free region would significantly improve if the continuum emission was removed first (i.e., if the sky subtraction was applied to Figure 1b instead of 1a), but the residuals in the region of interest for RC extraction would be unchanged. This result can be greatly improved by subtracting a sky line *template* spectrum, specifically constructed for MCG-2-31-017, from the continuum-free spectrum shown in Figure 1b. The sky template is a spectrum that contains only sky lines, with positions and intensities that match those in Figure 1b as closely as possible, at least near the $H\alpha$ line. It is obtained by taking the median of the continuum-subtracted spectra of three or more *reference* galaxies, showing no line emission in the redshift region where the $H\alpha$ line of the target galaxy lies. Each reference spectrum must be precisely aligned with the target spectrum to match the positions of its sky lines (with an accuracy of a few tenths of a pixel). Finally, the intensities of the template sky lines are optimized for the target spectrum by multiplying the template by a small numeric factor. Such factor is chosen upon examination of the residuals of the template subtraction near the $H\alpha$ line. If the residuals are positive for some sky lines and negative for others, the scaling factor used is that providing the most reliable RC (in this sense, a sky line residual running across the brightest part of the $H\alpha$ line does not affect the RC, whereas one that overlaps with the low signal-to-noise parts does). The identification of suitable reference galaxies can be very challenging, because not only the intensity of each sky line changes (depending on integration time and atmospheric conditions), but also the relative intensity of different sky lines can vary significantly over the course of the same night. More details on the choice of reference spectra can be found in Catinella (2005). The result of the template subtraction for MCG-2-31-017 is shown in Figure 1d: our method has substantially improved the quality of the sky subtraction. Figures 2a and 2b show the RCs extracted from the spectra in Figures 1c and 1d, respectively. The dotted lines

⁴ IRAF (Image Reduction and Analysis Facility) is distributed by the National Optical Astronomy Observatory, which is operated by the Association of Universities for Research in Astronomy (AURA) under cooperative agreement with the National Science Foundation.

indicate the center of symmetry of the RC, identified by the average of the 90th and 10th percentile velocities (kinematic center, discussed in § 4). The error bars are obtained from Gaussian fits to the $H\alpha$ line profile at each spatial position, as explained in § 3. A close inspection of Figure 2 shows that the RC in (b) is less noisy and traces slightly farther out than that in (a). The number of data points (112 and 104, respectively) affects the values of the percentile velocities used to identify the kinematic center, and accounts for the small offset (6 km s⁻¹) between the central velocities in the two cases.

In general, different templates are required for different objects, nights, or even different emission lines of the same galaxy, making this sky subtraction technique very time-consuming (unless the sky lines are fairly stable over a given night, in which case the same template might be used for multiple target spectra). Whether the result is worth the effort involved depends on the purpose of the observation and on the characteristics of the emission of the galaxy considered. In fact, the standard and template sky subtraction provide essentially the same RC width for MCG-2-31-017, but for galaxies with fainter $H\alpha$ emission, or for purpose of studying the details of the RC in its outer parts especially, this template fitting technique can produce a more robust measurement than the standard approach.

It is interesting to mention another approach to a similar sky-subtraction issue, developed by Bershadly et al. (2005, hereafter B05) for integral-field fiber spectroscopy. The subtraction of night sky emission for multifiber data has been a long-standing problem, usually dealt with by adopting observing techniques in which the telescope is nodded between targets and adjacent sky positions. This strategy is successful but not very efficient, since only half of the observing time is spent on the targets. An alternative solution based on a different sky subtraction algorithm has been recently proposed and tested on spectra obtained with SparsePak, a formatted fiber array optimized for spectroscopy of low surface brightness galaxies, described in Bershadly et al. (2004). Following the approach explained in detail in B05, the wavelength-calibrated and rectified multifiber spectra obtained from each observation are arranged into a two-dimensional image format, sorted by position along the slit (with the interfiber gaps taken out). The result is analogous to, and processed as, a long-slit spectrum. As Figure 14 of B05 shows, the problem is similar to that discussed in this section: the source line emission spans the whole extent of the slit, making the subtraction of the sky lines very difficult. In the case of the SparsePak observations, 7 of the 82 fibers were assigned to sky. Sky subtraction schemes that rely on a very small number of sky *pixels*, however, yield noisy results, similar to those shown in Figure 2c for our dataset. A significant improvement is obtained by using all the spatial channels (fibers): the spectrum is continuum-subtracted first (as we do for our spectra before template subtraction), and a low-order polynomial is then fit to each spectral channel, with a clipping algorithm that rejects spatial channels with source flux. This algorithm can be applied to continuum-subtracted long-slit spectra, provided that (a) there are enough source-line-free pixels at each wavelength to constrain the fit to the sky line profile, and (b) the shape of the sky line pro-

files is symmetric with respect to the center of the slit (so that the sky line fit over half slit fairly matches the other half). The second condition is certainly met by our Palomar spectra. In fact, for galaxies with line emission spilling over *one side only* of the slit, we removed the sky lines by fitting a *first-order* polynomial using only the signal-free side of the spectrum (if there were enough pixels to do so). When this method is applicable, it produces final spectra that are generally cleaner than those obtained via template subtraction.

In conclusion, both B05 and our template approaches can provide a significantly improved sky subtraction for long-slit spectra where the galaxy emission fills the slit. Which method should be used depends on the characteristics of the source emission – whereas B05’s algorithm avoids all the complications associated with the construction of a sky template (the choice of suitable reference galaxies, image registration, and intensity rescaling), its application requires a large enough number of signal-free pixels at each wavelength to constrain the sky line fits.

3. ROTATION CURVE EXTRACTION

Once continuum and sky line subtracted, the spectra are ready for RC extraction. Since the typical seeing at the Palomar Observatory is $\sim 1''\text{-}2''$, and the CCD spatial scale used was $\sim 0.5''$ pixel⁻¹, the RCs are clearly oversampled. Therefore, we Hanning smoothed the spectra and recorded the peak value of the velocity (from a Gaussian fit across the $H\alpha$ line) for every other pixel. The errors on the peak velocities were obtained through a Monte-Carlo resampling technique (an algorithm used by non-linear fitting *tasks* in IRAF to estimate coefficient errors): each section across the spatial axis of the Hanning-smoothed spectrum was replicated 15 times, each point being replaced by its value from the Gaussian fit plus noise with dispersion given by the RMS of the fit. A Gaussian fit was performed for each replication, and the dispersion of the fitted peak values used to estimate the velocity errors. All the points of the extracted RC were individually inspected, with particular attention to those belonging to low signal-to-noise regions, and only those with reliable Gaussian fits were kept. The profile of the $H\alpha$ line at each spatial position is usually well approximated by a Gaussian, with the possible exception of the innermost parts of the galaxies, where non-circular motions sometimes cause secondary peaks and deviations from the Gaussian shape (however such regions are typically those with the strongest $H\alpha$ emission, and therefore the positions of the profile peaks are well determined).

RCs with strong continuum emission or central bars, which mostly arise in earlier type (Sa-Sb) spirals, often show $H\alpha$ absorption in the nuclear regions, due to the strong Balmer absorption features of A-type stars. In these cases, we used another emission line, typically $[\text{NII}]\lambda 6584 \text{ \AA}$ if available, to fill in the central gaps of the $H\alpha$ RC. The $[\text{NII}]\lambda 6584 \text{ \AA}$ and $H\alpha$ RCs were extracted separately, matched, and the $[\text{NII}]\lambda 6584 \text{ \AA}$ data points kept only if lying within $H\alpha$ gaps. We applied a $[\text{NII}]\lambda 6584 \text{ \AA}$ patch to approximately 15% of our $H\alpha$ RCs.

When offset observations of the same galaxy (at the same slit position angle) were available, the RCs separately extracted from each spectrum were combined by matching their common features. In the region where

the RCs overlap, we did not average the data points, but rather keep the ones with higher signal-to-noise ratio. As an aside, we point out that since offset observations farther from the galaxy center were typically integrated for a longer time, a stronger feature (i.e., smaller error bars) in the combined RC does not necessarily represent a stronger intensity of the underlying HII regions.

4. ROTATION CURVE FOLDING

In order both to measure the velocity width using our algorithm (see § 5) and to determine the systemic recessional velocity, the rotation curves must be folded about a central origin, typically chosen as either the *photometric* center-of-light, or the *kinematic* center. The definition of the latter itself varies; one common method identifies the folding center with the velocity closest to the average of V_{10} and V_{90} , the 10th and 90th percentile points of the RC velocity histogram (notice that since there are no spatial interpolations involved, the two sides of the folded RC are sampled on the same spatial grid). As shown by Dale et al. (1997), kinematic centering appears preferable in most cases, because it avoids misidentification of the photometric center due to bars or extinction within the galaxy. Moreover, the estimate of the light peak position is very poor in galaxies with a weak or nearly absent continuum emission (16% of our sample), and in galaxies with nuclear regions dominated by H α absorption (15% of our sample). On the other hand, if a RC is significantly asymmetric or unevenly sampled (as in the case of galaxies that required offset observations), the kinematic centering will also provide an unsatisfactory folding. This is shown in Figure 3a for MCG-3-05-008 (AGC 410269), a galaxy with a rising RC, where the H α emission is traced farther out in one of the arms.

A better result can be obtained making use of the detailed shape of the RC by fitting an anti-symmetric function to the unfolded RC and leaving the spatial position and velocity of the center as free parameters. For its convenience and in order to minimize the number of fitting parameters, we adopt the *Universal Rotation Curve* (URC) description proposed by Persic et al. (1996) which incorporates contributions both from a stellar exponential thin disk and a spherical dark matter halo. Although inadequate to model individual RCs as already pointed out elsewhere (e.g., C97; Willick 1999), the URC provides a useful parameterization of the *average* RC of a galaxy in terms of its luminosity and optical radius R_{opt} . In particular, the URC description approximates the overall shape of a RC adequately for the purpose of determining its center of symmetry.

In order to apply the URC folding method, we make use of the detailed SFI++ I-band photometric data available to us, assigning to each galaxy its corresponding URC model based on its I-band luminosity, R_{opt} , and inclination, and leave a scale factor and a small offset from the kinematic center, in both radial and velocity directions, as free parameters determined via a non-linear least square fit to the RC data points. Figure 3b demonstrates that this technique (*URC folding*) is remarkably more successful than the simple kinematic one based on the histogram method, shown in (a), at folding asymmetric RCs. As expected, for symmetric RCs the two folding methods give essentially the same result. As discussed in § 5, we measure the rotational velocity of a disk

galaxy at R_{opt} from a functional fit (*Polyex* model, also shown in Figure 3b) to its folded RC. It should be noted that the RC folding is not strictly necessary for this type of width measurement, but the identification of the RC center cannot be avoided. In fact, other authors prefer to add two parameters to the expression used to model a RC, solving for its shape and center at the same time (e.g., C97).

In order to assess the comparative validity of the kinematic and URC folding techniques on a quantitative basis, we make use of the larger SFI++ sample and test their respective ability to minimize the asymmetry of the folded RCs. As a measure of asymmetry, we adopt the definition given by Dale & Uson (2003):

$$\text{Asymmetry} = \sum \frac{||V(R)| - |V(-R)||}{\sqrt{\sigma^2(R) + \sigma^2(-R)}} \times \left[\frac{1}{2} \sum \frac{|V(R)| + |V(-R)|}{\sqrt{\sigma^2(R) + \sigma^2(-R)}} \right]^{-1} \quad (1)$$

where $V(R)$ and $\sigma(R)$ are velocity and corresponding uncertainty at the radial position R , and the summation symbols refer to radial distances for which *both arms* are sampled (unpaired RC data points are excluded). The quantity defined in Equation 1 simply measures the area between the two folded RC arms, normalized by the average area that they subtend. The calculation of the asymmetry index is slightly more complicated for the URC-folded RCs, because in general the two arms are *not* sampled on the same spatial grid (due to a small spatial offset from the kinematic center). We therefore calculate two indices for each RC by pairing the points on one arm with those obtained by interpolation of the other arm at the same spatial positions, and take their average as our measure of asymmetry.

The distributions of the URC and kinematic asymmetry indices of the 999 optical RCs with available velocity error information in our digital archive are presented in Figure 4. The histogram obtained for the URC folding (solid) is more centrally concentrated than the one corresponding to kinematic folding (hatched), indicating that the first technique is more effective at minimizing the overall asymmetry of the RCs. The mean asymmetry indices for the URC and kinematic cases are $11.3 \pm 0.3\%$ and $19.4 \pm 0.5\%$, respectively; for comparison, Dale et al. (2001, hereafter D01) obtained an average asymmetry of $12.5 \pm 1.0\%$ applying Equation 1 to a sample of field galaxies (in the foreground or background of clusters) with RCs folded according to the kinematic histogram technique. Both D01 and our samples were selected for TF studies, have similar morphological composition (dominated by normal late-type spirals, mostly Sc), and were obtained with similar instrument setup (most of the D01 spectroscopy was carried out with the Palomar 5m telescope); however the characteristic redshift of our galaxies is smaller (typically $z \lesssim 0.03$, as opposed to $0.02 \lesssim z \lesssim 0.08$ for D01). The loss of spatial detail of the RCs of the more distant galaxies probably accounts for the smaller asymmetry index obtained by D01 using the histogram technique. The folding of spatially well-sampled RCs should be done by taking into account the RC shape. Folding algorithms that rely on velocity histograms alone might in fact introduce spurious asymmetry in the folded RC due to non-optimal matching of

the two arms, as shown in Figure 3 (the URC and kinematic asymmetry indices for that RC are 0.17 and 0.74, respectively).

RC asymmetry indices have been derived in this section with the limited intent of comparing the two folding techniques. It should be noted however that the asymmetry parameter itself could be used to determine the folding, its minimum value identifying the center of symmetry of the RC. For RCs that are well-sampled and traced to similar extent on both sides, we expect this and our method to give similar results, since fitting the URC is effectively a way of minimizing the overall asymmetry of the RC. For other cases, however, the URC technique has an important advantage: *all* the RC points are used to determine the folding center and not only those lying at radial distances that are sampled on both sides of the RC. In particular, our technique provides a satisfactory result for galaxies (a) with patchy H α emission or (b) with the two sides unevenly sampled (as it happens for our offset observations). While in case (b) the asymmetry index centering might still yield a good result (even if using a smaller number of RC points), there are examples of case (a) where the asymmetry index could not be calculated (e.g., AGC 4271 and AGC 221928 in Figure 5; see § 6).

A complete treatment of asymmetry in RCs, as well as a more general comparison among folding techniques, are beyond the scope of this paper, and will be addressed in a future work.

5. RC WIDTH MEASUREMENT

As discussed e.g., by C97 and Raychaudhury et al. (1997), algorithms to measure rotational velocities from RCs can be divided into two principal categories: *histogram* and *model* widths. The former are obtained by collapsing the RCs into velocity histograms, and calculating the difference between V_N and V_{100-N} , where V_N is the N-th percentile velocity (typically, N=10). This or similar definitions have been adopted by, e.g., Mathewson et al. (1992), Mathewson & Ford (1996), Vogt (1995), and Vogt et al. (2004a). Model widths are measured at a fixed galactocentric distance (derived from photometry) from model fits to the RCs. A number of different fitting functions have been adopted such as those discussed by C97; since they are all empirical, trade-offs between simplicity and detail result. Authors who have published large collections of model widths include C97, Dale (1998), and Dale et al. (1997, 1998, 1999a,b,c, 2001). Histogram widths are easier to measure and do not require accompanying photometry, but do not make use of the spatial information contained in the RCs, and therefore, not surprisingly, they are inferior to the model widths. A direct comparison between the two types of widths shows in fact that the histogram ones are affected by biases that correlate with the shape and extent of the RCs (Paper II). For example, histogram widths derived from RCs with an extent $R_{\max} \leq R_{\text{opt}}$ are typically smaller than model widths measured at R_{opt} , the difference being larger for smaller R_{\max}/R_{opt} ratios and steeper RCs (for rising RCs, the average width difference is 20 km s $^{-1}$ or larger, depending on RC extent). When heterogeneous width measurements are used in a TF survey, systematic trends such as the one described must be taken into account in order to avoid biases in the

analysis. For instance, a width difference of 20 km s $^{-1}$ translates into approximately a 0.2 mag offset on the TF plane, or 500 km s $^{-1}$ in peculiar velocity, at $cz \sim 5000$ km s $^{-1}$. Clearly, galaxies of different measures will be mixed in a statistical sample, and the net effect will be reduced. However, if the data sets are segregated in sky coverage, spurious bulk flows of significant size can arise as a result.

The method adopted here to determine velocity widths involves fitting a function (*Polyex* model; Giovanelli & Haynes 2002) to the folded RC, and measuring the velocity from the fit, at the optical radius R_{opt} of the galaxy. The RC is folded using the URC technique described in § 4. As its name suggests, the functional form of the Polyex model combines an exponential, which follows the inner RC rise, and a polynomial, which reflects the outer RC slope:

$$V_{\text{PE}}(r) = V_0(1 - e^{-r/r_{\text{PE}}})(1 + \alpha r/r_{\text{PE}}) \quad (2)$$

where V_0 , r_{PE} , and α determine the amplitude, the exponential scale of the inner region, and the slope of the outer part of the RC, respectively. The Polyex width is thus simply defined as $W_{\text{PE}} = 2 V_{\text{PE}}(R_{\text{opt}})$. An example of the Polyex width measurement technique for a representative galaxy is presented in Figure 3b.

Considerable discussion has appeared in the literature concerning the spatial position at which the RC width should be measured in light both of the relevant physics and practical concerns about fitting disk scale lengths and possible extinction effects. Following, e.g. C97, many authors adopt the location of the peak rotational velocity for a pure exponential disk, $r_{\text{disk}} = 2.15 h$, where h is the disk scale length. As mentioned previously, the inclusion of an extensive dark matter halo eliminates such a predicted RC peak. Furthermore, several studies (Giovanelli & Haynes 2002; Baes et al. 2003; Valotto & Giovanelli 2004) have demonstrated clear evidence that extinction can significantly affect the inner slopes of observed rotation curves with the impact being dependent on the galaxy's intrinsic luminosity. For these reasons, we elect to measure further out in the disk, at R_{opt} . It should be noted that we measure R_{opt} as the radius containing 83% of the total light, not at a fixed number of scale lengths (Haynes et al. 1999). Further discussion of this issue is addressed in Paper II, where our width measurement technique is compared to others proposed in the literature.

In those cases for which the RC does not reach R_{opt} , application of this method requires an extrapolation of the fit beyond the last measured point. As discussed further in Paper II, such extrapolation produces reliable velocity widths only when $R_{\max}/R_{\text{opt}} \geq 0.5$, where R_{\max} is the RC extent (i.e., the maximum radial distance up to which the folded RC is sampled). Because our observations have typically been made with the Hale 5m telescope, they are of high sensitivity. In practice, the Polyex function has enough flexibility to fit the vast majority (~94%) of the individual RCs in the SFI++ dataset (including those that are declining at large radii). Finally, it is worth mentioning that Equation 2 is not based on any physical models of the velocity field of disk galaxies, but only represents a convenient, empirical expression to fit a large variety of RC shapes.

Observed velocity widths derived from RCs must be

corrected for cosmological broadening (to obtain the rest-frame velocities) and deprojected to an edge-on view:

$$W^{\text{corr}} = \frac{W^{\text{obs}}}{(1+z) \sin i} \quad (3)$$

where z and i are redshift and inclination to the line of sight of the galaxy, respectively. Total errors on velocity widths typical of RC datasets considered here are of the order of 20 km s^{-1} (Giovanelli et al. 1997a).

6. DATA PRESENTATION

Table 1 lists the main parameters of the 403 galaxies for which final, extended ($R_{\text{max}} \geq 0.5 R_{\text{opt}}$) RCs have been obtained, ordered by increasing Right Ascension. We show here only the first page to illustrate form and content⁵. The parameters listed are:

Col. 1: identification code in our private database, referred to as the Arecibo General Catalog (AGC). If a galaxy is also listed in the UGC catalog (Nilson 1973), its UGC and AGC codes are identical.

Col. 2: NGC or IC designation, or other name, typically from the CGCG (Zwicky et al. 1961-68) or MCG (Vorontsov-Velyaminov & Arhipova 1968) catalogs. CGCG numbers are listed in the form: field number-ordinal number within the field; MCG designations are abbreviated to eight characters.

Cols. 3 and 4: Right Ascension and Declination for the epoch J2000.0. Coordinates have been obtained from the Digitized Sky Survey catalog and are accurate to within $2''$.

Col. 5: T, morphological type code according to the scheme in the RC3 catalog (de Vaucouleurs et al. 1991); code 1 corresponds to Sa, code 3 to Sb, code 5 to Sc, etc. A “B” following the type code indicates the presence of an identifiable bar.

Col. 6: R_{opt} , optical radius in arcsec, corresponding to the isophote that includes 83% of the I-band flux.

Col. 7: R_{max} , maximum radial distance to which the folded RC is sampled, in arcsec.

Cols. 8–10: parameters of the Polyex fit (see Equation 2) to the folded RC.

Col. 11: flag that indicates the quality of the Polyex fit. The flag is set to 1 if the fit is deemed good or acceptable, and to 0 if the fit is poor.

Col. 12: heliocentric velocity from the RC velocity histogram, $V_{80} = (V_{10} + V_{90})/2$ (§4).

Col. 13: velocity width from the RC velocity histogram, $W_{80} = V_{90} - V_{10}$, corrected for cosmological broadening only (§5).

Col. 14: V_{PE} , heliocentric velocity from the Polyex fit and its uncertainty (estimated from the fit to the RC data points).

Col. 15: W_{PE} , velocity width from the Polyex fit, corrected for cosmological broadening only (§5), and its estimated uncertainty.

The empty entries in the Table (columns 6–11, 14, and 15) refer to 44 galaxies for which good quality photometry was not available (14 of which without an I-band image) and therefore, for which a Polyex width could not be measured.

⁵ Table 1 is available in its entirety in the electronic edition of the Journal.

In Figure 5, we show the corresponding $\text{H}\alpha$ RCs⁶, Hanning-smoothed and recorded every other pixel to account for oversampling (see §3). The AGC identification code is given in each panel. In one case (AGC 12591) the RC was obtained from the $[\text{NII}]\lambda 6584 \text{ \AA}$ emission line (which was stronger and slightly more extended than $\text{H}\alpha$). The RCs are folded according to the URC technique explained in §4, and *not* deprojected to an edge-on view. The solid line shows the Polyex fit, and the vertical dashed line indicates the position of R_{opt} , where the Polyex width is measured. The adopted half velocity width is indicated by the horizontal line. In those cases where a Polyex fit was not available due to lack of photometry, the folding was done about the position of the kinematic center (see §4).

7. DEPENDENCE OF RC EXTENT ON HI CONTENT

One of the factors that directly determine the observed rotational velocity of a galaxy is the radial extent within the disk out to which the adopted kinematic tracer is detectable. For example, the velocity width of a galaxy with a rising RC, as measured from an HI global profile, will underestimate the true value if the distribution of the neutral hydrogen is truncated (a situation that is typical for objects located in high density regions such as centers of clusters). RC widths obtained by means of velocity histograms in spatially resolved data – a method that closely resembles that used to measure radio widths from HI integrated line-profiles, although not intensity-weighted – will suffer the same bias if the tracer is truncated. The impact of a possible $\text{H}\alpha$ truncation on RC model widths is expected to be negligible, since the measurement is performed at a fixed galactocentric distance, provided that the RC is extended enough to allow for a reliable fit of its shape; nonetheless, such expectation should be carefully investigated.

Several studies have already provided evidences for the existence of a correlation between $\text{H}\alpha$ and HI extents, most notably for galaxies in the Virgo cluster (e.g., Koopmann & Kenney 1998; Rubin et al. 1999). This is also in agreement with previous findings of truncated star formation in HI deficient spirals. For instance Haynes & Giovanelli (1986) found that HI poor galaxies in the Virgo cluster are redder than those of similar morphology but normal HI content, and concluded that the star formation has been quenched in those objects. Gavazzi et al. (2002) reached the same conclusion based on spectral energy distribution modeling of spectrophotometric data of a rich sample of spirals in Virgo. More recently, Vogt et al. (2004b) studied a sample of 296 in-falling spirals selected from 18 nearby clusters (and 33 isolated field galaxies for comparison) and showed that the distributions of HI flux and of HII regions within the disks are clearly correlated.

Here, we make use of the entire SFI++ dataset, which is not restricted to cluster galaxies, to investigate the dependence of the extent of the $\text{H}\alpha$ emission on HI content. The SFI++ compilation contains 715 galaxies which have good quality optical RCs and HI flux measurements (Springob et al. 2005). We follow the common practice of defining the comparative HI content, $\langle \text{HI} \rangle$, as

⁶ A complete set is available in the electronic edition of the Journal.

the difference, in logarithmic units, between the observed HI mass, $M_{\text{HI}}^{\text{obs}}$, and the value expected for an isolated galaxy of the same morphological type, T^{obs} , and optical linear diameter, $D_{\text{opt}}^{\text{obs}}$ (Haynes & Giovanelli 1984; Solanes et al. 2001):

$$\langle \text{HI} \rangle = \langle \log M_{\text{HI}}(T^{\text{obs}}, D_{\text{opt}}^{\text{obs}}) \rangle - \log M_{\text{HI}}^{\text{obs}} \quad (4)$$

where M_{HI} is in solar units and D_{opt} in kpc. This definition is commonly referred to as the *HI deficiency* and is used to identify truly HI poor objects. Note that in these units, objects with $\langle \text{HI} \rangle > +0.3$ are HI deficient by a factor of 2 relative to similar isolated galaxies, and those with $\langle \text{HI} \rangle > +0.5$ by a factor of 3. It should also be noted that values of $\langle \text{HI} \rangle$ for individual objects are very uncertain (Solanes et al. 2001) and therefore this quantity should be calculated for a data set and interpreted in a statistical fashion. We used the equations in Solanes et al. (1996, hereafter SGH96) to calculate the observed HI mass from the corrected HI flux (obtained from Springob et al. 2005) and the linear diameter from the apparent blue visual size (using the velocity in the CMB frame to estimate the radial distance). In particular, we used the maximum likelihood linear regressions of $\log(h^2 M_{\text{HI}})$ on $\log(h D_{\text{opt}})$ (where h is the Hubble constant in units of $100 \text{ km s}^{-1} \text{ Mpc}^{-1}$) presented in Table 2 of SGH96 to calculate the expectation value of the HI mass in Equation 4. The regression relations are given only for the morphological types Sa+Sab, Sb, Sbc, Sc, and All; we thus assigned: S0a same as Sa, Scd-Sd same as Sc, and other types same as All.

From among the galaxies with good quality RCs in SFI++, we extracted two subsets: those with good HI-line emission profiles (715 objects) and those that were marginally or non-detected in HI (27 objects). We calculated the HI content $\langle \text{HI} \rangle$ as defined above for the first subset. For the second group, we obtained lower limits using upper limits to the estimated HI mass, which is commonly calculated (e.g., SGH96) by assuming a rectangular HI emission profile of amplitude 1.5 times the observed RMS noise per channel and a typical rotational width (since a RC was available for each galaxy, we used the Polyex width).

The distribution of $\langle \text{HI} \rangle$ is shown in Figure 6a for both detections (solid histogram) and marginal or non-detections (hatched histogram; the numbers are multiplied by 5). The dotted line at $\langle \text{HI} \rangle = 0.3$ separates HI-poor (right) from HI-normal or HI-rich galaxies (left). As noted previously (e.g., Vogt et al. 2004b) most of the truly HI deficient objects are not detected in HI, are found in cluster cores, and have truncated HI and H α disks. Such objects make up only a small fraction of the SFI++ RC sample. The significant new result is shown in Figure 6b, where the RC extent (i.e., the maximum radial distance R_{max} out to which the folded RC is sampled, relative to the optical radius R_{opt}) is plotted as a function of $\langle \text{HI} \rangle$ for the overall sample. The correlation between these two quantities, noted by previous authors in the case of HI-stripped spirals in clusters (and confirmed by our sample, although the number of HI-poor objects is very small) *continues among the HI-normal galaxies*, in the sense that objects with lower than average HI mass also have smaller than average H α disks. Since both $\langle \text{HI} \rangle$ and $R_{\text{max}}/R_{\text{opt}}$ are normalized quantities, this correlation is not a simple scaling relation.

These results are important for the interpretation of systematic trends observed when velocity widths obtained from HI integrated line profiles and long-slit optical RCs (using both histogram and model approaches) are compared. As mentioned at the beginning of this section, we would expect RC model widths to be negligibly affected by H α truncation (as long as the extrapolation to R_{opt} is deemed reliable). However the difference between HI and Polyex widths does show a weak dependence on RC extent (normalized to R_{opt}), in the sense that larger width differences are observed for galaxies with H α emission traced farther out in the disk (Paper II; Catinella 2005). This bias is important for galaxies with steeply rising RCs, and can be explained by the correlation between H α and HI disk sizes discussed here, which – for rising RCs – implies larger HI widths for galaxies with more extended H α emission. These results will be further discussed in Paper II, where the width comparison will be presented in detail, and statistical corrections will be determined with the purpose of making rotational velocities for TF work technique-independent.

8. SUMMARY

Here, we have presented new long-slit optical emission line RCs for 403 galaxies and have derived from them rotational widths of particular use for applications of the TF relation. We described the RC extraction process and illustrated a method to subtract the night sky lines from spectra which contain emission well extended along the spectrograph slit. For galaxies with such extended emission, this *template* sky subtraction technique yields RCs that are less noisy than those obtained with the standard sky removal method, thus allowing one to sample the velocity field to a larger spatial extent, especially when the galaxy line emission is faint. Our approach to determine the center of symmetry about which the RC folding is performed exploits use of the URC model and knowledge of the galaxies photometric properties from I-band imaging observations. The measurement of rotational velocity involves fitting an empirical function, the Polyex model, to the folded RC and measuring the velocity from such fit, at R_{opt} , the radius encompassing 83% of the total I-band light.

Because of its relevance to the measurement of rotational widths from long-slit RCs, we have studied the relation between HI content and RC extent for 742 galaxies in the SFI++ sample, for which both measurements are available (for 27 objects marginally or non-detected in HI, lower limits for the HI content have been derived). We found a clear correlation, in the sense that a larger than average HI content implies a larger than average H α disk relative to the optical size. In addition to confirming previous findings of H α truncation in HI-poor cluster galaxies, our results show that the trend holds for HI-normal, field objects: for a given optical size, star formation can be traced further out in the disks of galaxies with larger HI mass.

The RC data presented complement other data for a large sample of several thousand disk galaxies for which I-band photometry and H α or HI-line spectroscopy are available. This combined SFI++ dataset is being used to investigate the peculiar velocity field in the local universe via application of the TF method as well as to perform detailed statistical studies on the nature of disk gala-

xies. The detailed comparison between our and other RC width determinations as well as the cross-calibration of optical and global HI line rotational velocity measures will be presented in Paper II. The same dataset is being used to derive average or *template* RCs in bins of galaxy luminosity, which provide the basis for comparative study of possible variations in the kinematic properties of disk galaxies with increasing redshift (Catinella 2005; Catinella et al. 2005a).

⁷ NED is operated by the Jet Propulsion Laboratory, California Institute of Technology, under contract with the National Aeronautics and Space Administration.

⁸ SkyView was developed and is maintained under NASA ADP

This research was supported by NSF grants AST-9900695, AST-0307396 and by a NAIC pre-doctoral research grant at the Arecibo Observatory to B.C. We wish to thank the referee Matthew Bershadly for helpful comments on the manuscript. We acknowledge the use of NASA/IPAC Extragalactic Database (NED)⁷ and NASA's SkyView facility⁸.

Grant NAS5-32068 under the auspices of the High Energy Astrophysics Science Archive Research Center (HEASARC) at the Goddard Space Flight Center Laboratory of NASA.

REFERENCES

- Baes, M., et al. 2003, MNRAS, 343, 1081
 Bershadly, M. A., Andersen, D. R., Harker, J., Ramsey, L. W., & Verheijen, M. A. W. 2004, PASP, 116, 565
 Bershadly, M. A., Andersen, D. R., Verheijen, M. A. W., Westfall, K. B., Crawford, S. M., & Swaters, R. A. 2005, ApJS, 156, 311 (B05)
 Catinella, B. 2005, Ph.D. thesis, Cornell Univ.
 Catinella, B., Giovanelli, R., & Haynes, M. P. 2005a, ApJ, submitted
 Catinella, B., Haynes, M. P., & Giovanelli, R., 2005b, in preparation (Paper II)
 Chiba, M. & Yoshi, Y. 1995, ApJ, 442, 82
 Courteau, S. 1997, AJ, 114, 2402 (C97)
 Dale, D. A. 1998, Ph.D. thesis, Cornell Univ.
 Dale, D. A., Giovanelli, R., Haynes, M. P., Scodreggio, M., Hardy, E., & Campusano, L. E. 1997, AJ, 114, 455
 Dale, D. A., Giovanelli, R., Haynes, M. P., Scodreggio, M., Hardy, E., & Campusano, L. E. 1998, AJ, 115, 418
 Dale, D. A., Giovanelli, R., Haynes, M. P., Hardy, E., & Campusano, L. E. 1999a, AJ, 118, 1468
 Dale, D. A., Giovanelli, R., Haynes, M. P., Campusano, L. E., & Hardy, E. 1999b, AJ, 118, 1489
 Dale, D. A., Giovanelli, R., Haynes, M. P., Campusano, L. E., Hardy, E. & Borgani, S. 1999c, ApJ, 510, L11
 Dale, D. A., Giovanelli, R., Haynes, M. P., Hardy, E., & Campusano, L. E. 2001, AJ, 121, 1886 (D01)
 Dale, D. A., & Uson, J. M. 2003, AJ, 126, 675
 de Vaucouleurs, G., de Vaucouleurs, A., Corwin, H. G., Buta, R. J., Paturel, G., & Foqué, P. 1991, Third Reference Catalogue of Bright Galaxies (New York: Springer) (RC3)
 Freeman, K. C. 1970, ApJ, 160, 811
 Gavazzi, G., Bonfanti, C., Sanvito, G., Boselli, A., & Scodreggio, M. 2002, ApJ, 576, 135
 Giovanelli, R., & Haynes, M. P. 2002, ApJ, 571, L107
 Giovanelli, R., Haynes, M. P., Herter, T., Wegner, G., Salzer, J. J., da Costa, L. N., & Freudling, W. 1997a, AJ, 113, 22
 Giovanelli, R., Haynes, M. P., Herter, T., Vogt, N. P., da Costa, L. N., Freudling, W., Salzer, J. J., & Wegner, G. 1997b, AJ, 113, 53
 Haynes, M. P., & Giovanelli, R. 1984, AJ, 89, 758
 Haynes, M. P., & Giovanelli, R. 1986, ApJ, 306, 466
 Haynes, M. P., Giovanelli, R., Salzer, J. J., Wegner, G., Freudling, W., da Costa, L. N., Herter, T., & Vogt, N. P. 1999, AJ, 117, 1668
 Koopmann, R. A., & Kenney, J. D. P. 1998, ApJ, 497, L75
 Mathewson, D. S., & Ford, V. L. 1996, ApJS, 107, 97
 Mathewson, D. S., Ford, V. L., & Buchhorn, M. 1992, ApJS, 81, 413
 Navarro, J. F., Frenk, C. S., & White, S. D. M. 1997, ApJ, 490, 493
 Nilson, P. 1973, Uppsala General Catalogue of Galaxies, Acta Univ. Upsal., Ser. V:A, Vol. 1 (UGC)
 Oke, J. B., & Gunn, J. E. 1982, PASP, 94, 586
 Persic, M., Salucci, P., & Stel, F. 1996, MNRAS, 281, 27
 Raychaudhury, S., von Braun, K., Bernstein, G. M., & Guhathakurta, P. 1997, AJ, 113, 2046
 Rubin, V. C., Waterman, A. H., & Kenney, J. D. P. 1999, AJ, 118, 236
 Solanes, J. M., Giovanelli, R., & Haynes, M. P. 1996, ApJ, 461, 609 (SGH96)
 Solanes, J. M., Manrique, A., García-Gómez, C., González-Casado, G., Giovanelli, R., & Haynes, M. P. 2001, ApJ, 548, 97
 Springob, C. M., Haynes, M. P., Giovanelli, R., & Kent, B. R. 2005, ApJS, in press
 Tully, R. B., & Fisher, J. R. 1977, A&A, 54, 661
 Valotto, C., & Giovanelli, R. 2004, AJ, 128, 115
 Vogt, N. P. 1995, Ph.D. thesis, Cornell Univ.
 Vogt, N. P., Haynes, M. P., Herter, T., & Giovanelli, R. 2004a, AJ, 127, 3273
 Vogt, N. P., Haynes, M. P., Giovanelli, R., & Herter, T. 2004b, AJ, 127, 3300
 Vorontsov-Velyaminov, B. A., & Arhipova, V. P. 1968, Morphological Catalog of Galaxies (Moscow: Moscow State Univ.) (MCG)
 Willick, J. A. 1999, ApJ, 516, 47
 Zwicky, F., Herzog, E., Karpowicz, M., Kowal, C., & Wild, P. 1961-1968, Catalogue of Galaxies and Clusters of Galaxies, Vols. 1-6 (Pasadena: Caltech) (CGCG)

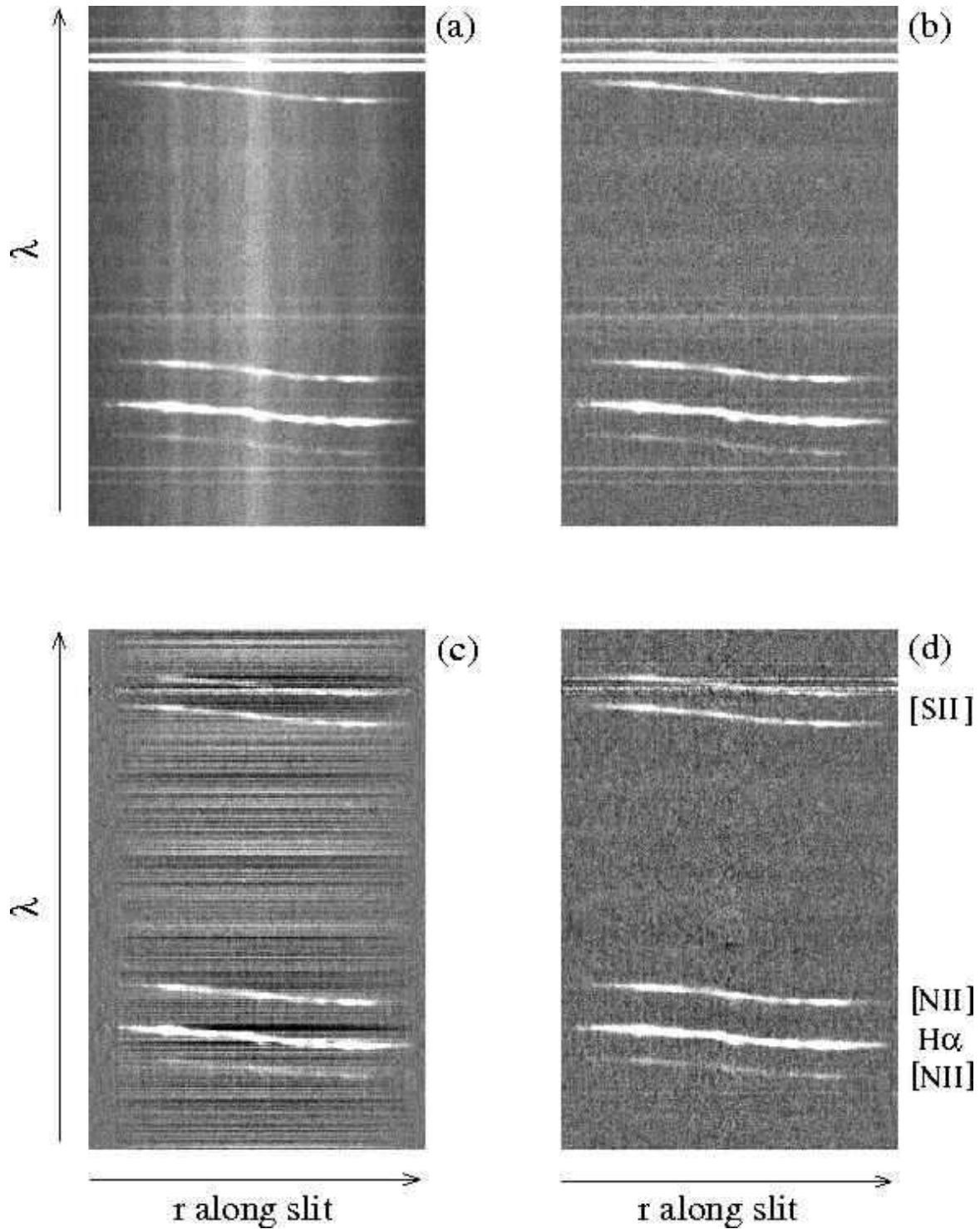


FIG. 1.— Demonstration of the template sky line subtraction process for MCG-2-31-017, a galaxy with line emission which fills the slit (we show here only the region with galaxy emission lines; the wavelength range runs approximately from 6610 to 6860 Å). Top panels: spectrum before (a) and after (b) galaxy continuum subtraction. Bottom panels: comparison between standard (c) and *template* (d) sky subtraction. In (d) the sky lines have been removed by subtracting a *sky line template* (see text). Different galaxies require, in general, different templates.

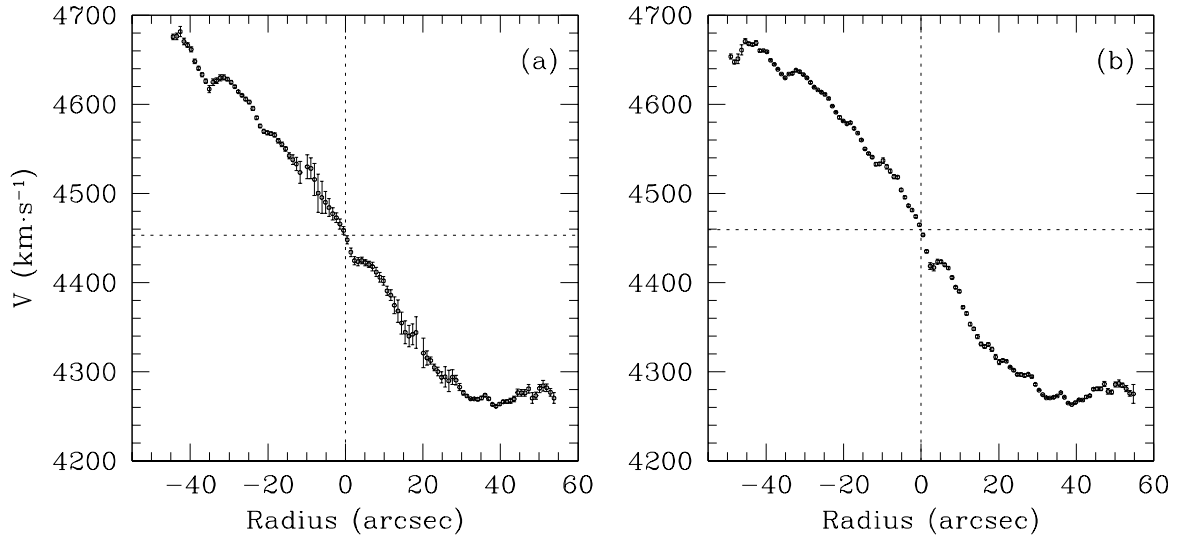


FIG. 2.— (a) $H\alpha$ RC of MCG-2-31-017, extracted from the sky line-subtracted spectrum in Figure 1c. The dotted lines mark the position of the kinematic center (see § 4, and Figure 3). (b) Same as (a), for Figure 1d. The large residuals present in Figure 1c result in larger error bars in (a) compared to (b).

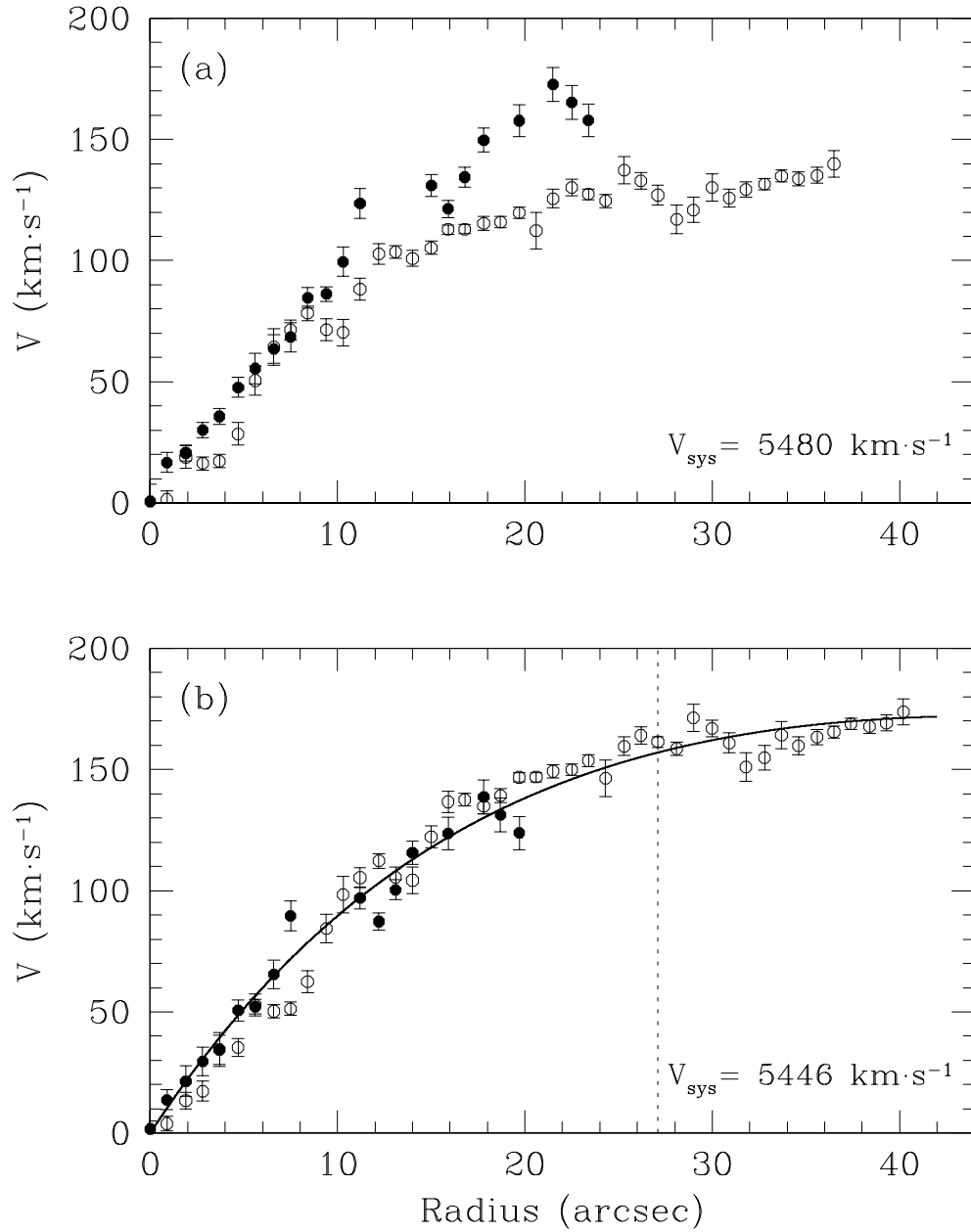


FIG. 3.— Comparison between kinematic (a) and URC (b) folding techniques for MCG-3-05-008. In (a) the RC center is identified by the data point with velocity closest to $V_{\text{sys}} = (V_{10} + V_{90})/2$, where V_N is the Nth percentile velocity. In (b) the center of symmetry has been determined by fitting a URC model to the unfolded RC. The best-fitting URC (not shown) indicates an offset of $-34 \text{ km}\cdot\text{s}^{-1}$ with respect to the kinematic center (no offset along the spatial direction), and provides a significantly better folding. The solid line in (b) shows the Polyex fit (Equation 2); the dotted line is at the optical radius, where the velocity width is measured. The RC is *not* deprojected to an edge-on view.

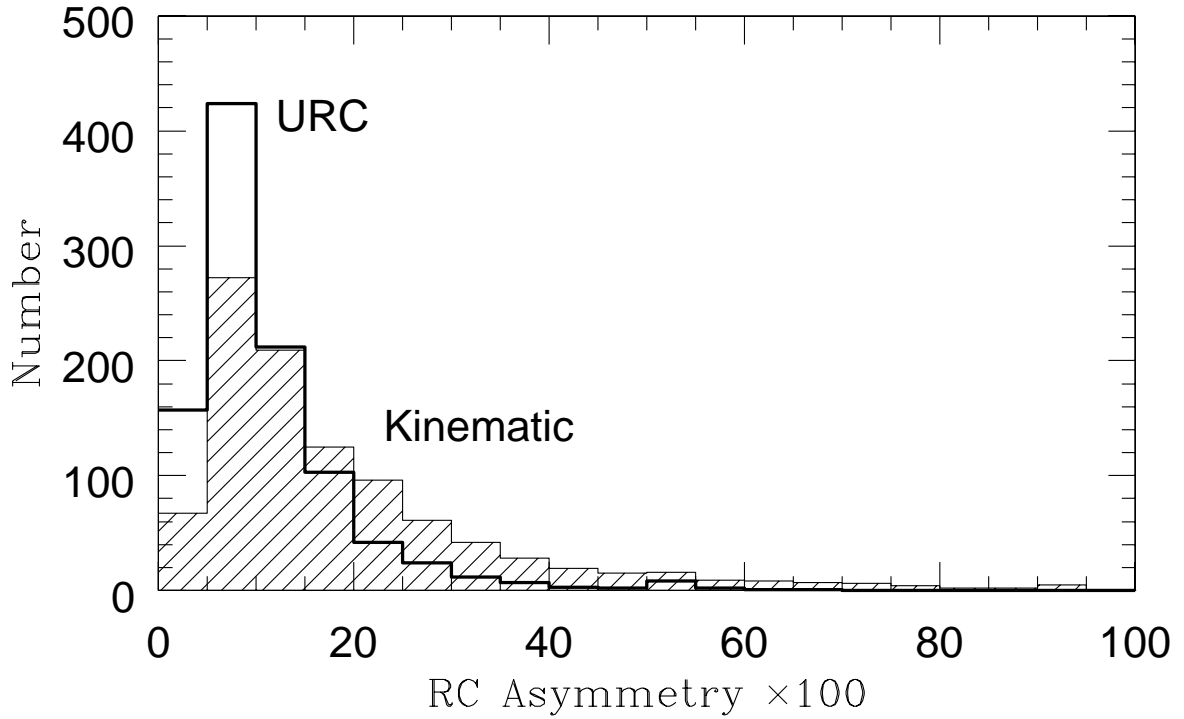


FIG. 4.— Distributions of the asymmetry indices for RCs folded according to the URC (solid histogram) or the kinematic (hatched histogram) techniques (see Figure 3). The two indices have been calculated for the optical RCs in our digital archive, for which velocity errors were also available (999 objects). The URC distribution is more centrally concentrated, and does not have a significant tail of high “RC asymmetry”, showing that this algorithm is more effective at minimizing the overall asymmetry of the folded RCs.

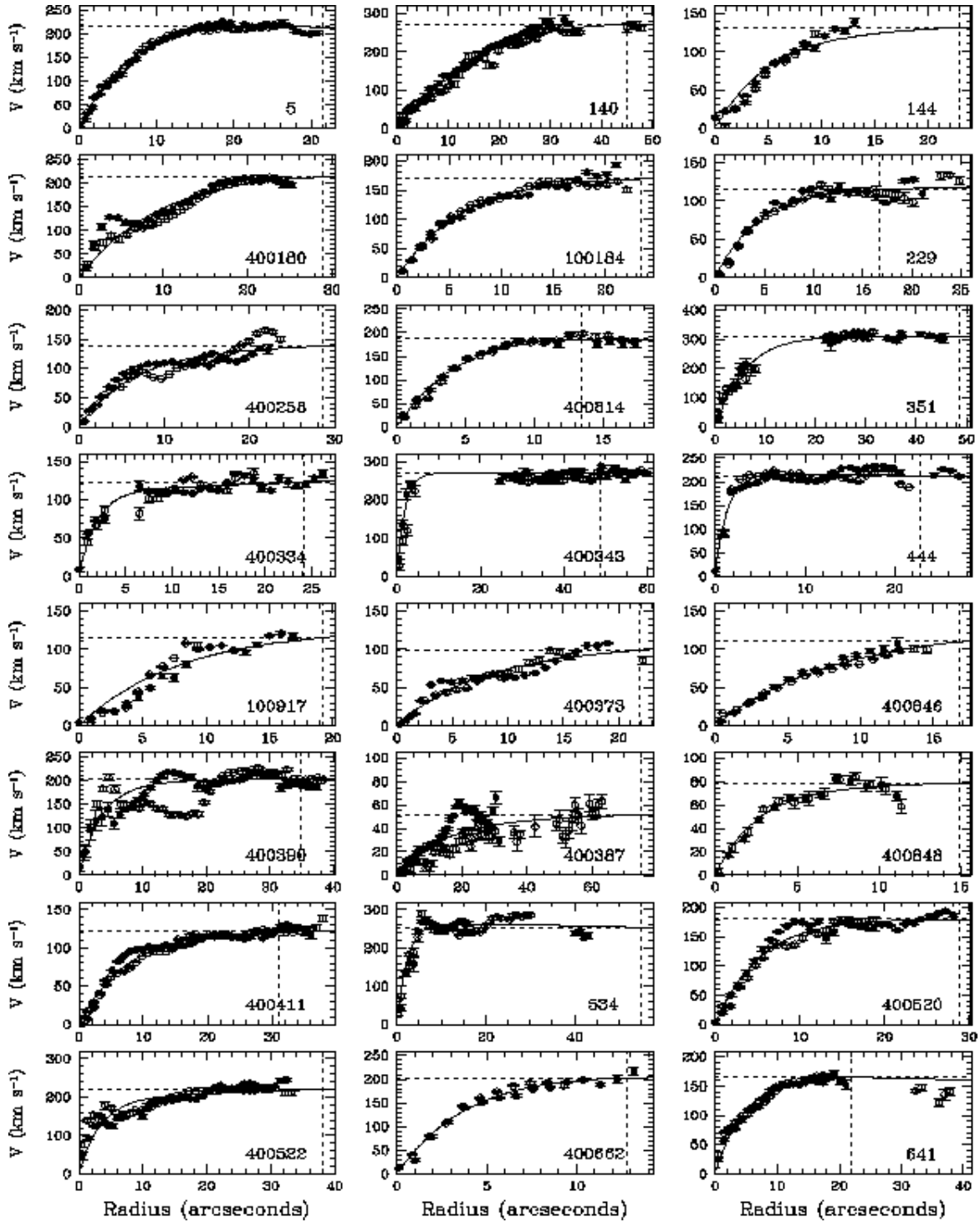


FIG. 5.— $H\alpha$ rotation curves, Hanning-smoothed and recorded every other pixel to account for oversampling. The AGC identification code is given in each panel. In one case (AGC 12591) the RC has been extracted from the $[NII]\lambda 6584 \text{ \AA}$ emission line. The error bars are formal errors from the Gaussian fits to the peak velocities. The RCs are *not* deprojected to an edge-on view. The Polyex fit is shown by a solid line; the dotted lines indicate the position of R_{opt} and the adopted half velocity width. We show here only the first page.

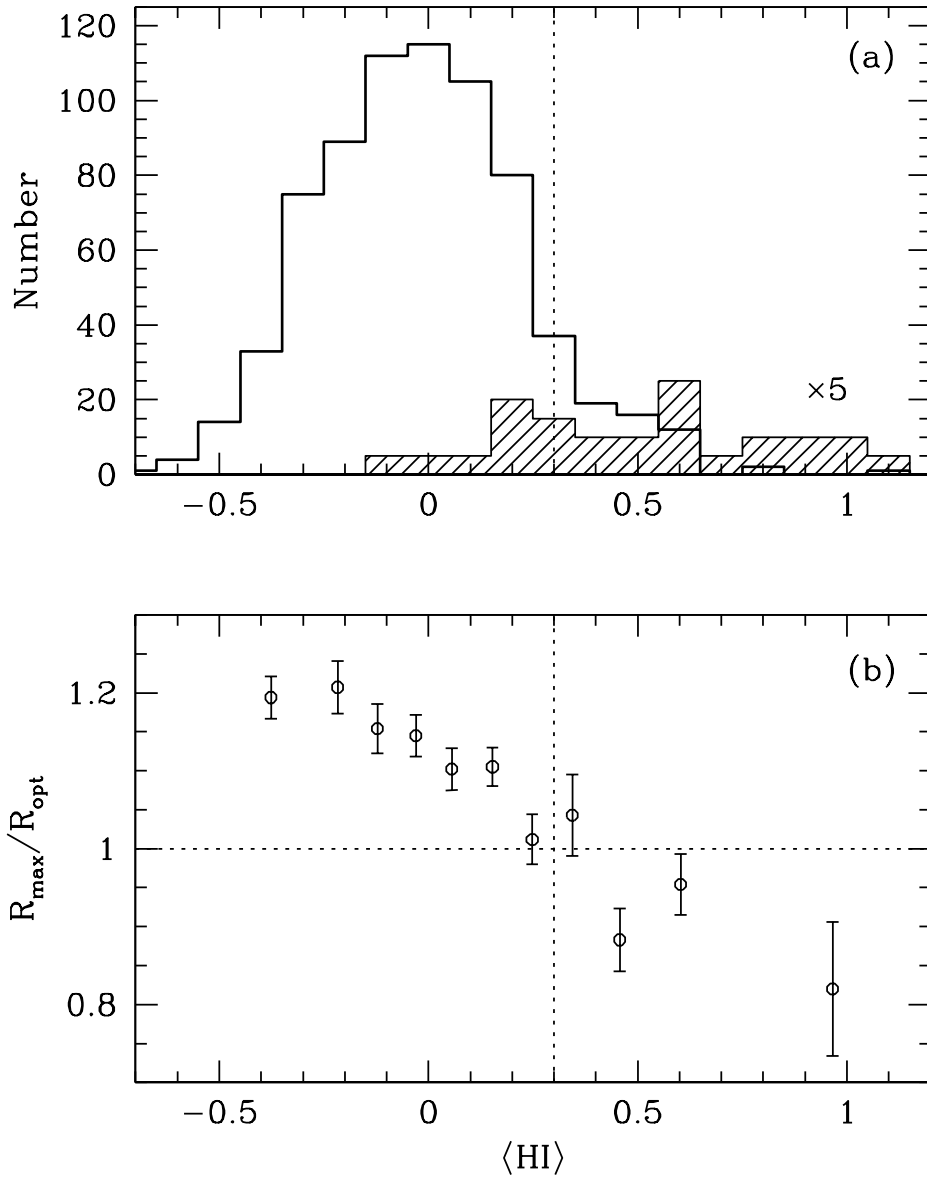


FIG. 6.— (a) HI content distribution for 715 SFI++ galaxies with optical RC and HI emission profile (solid histogram), and for 27 marginal or non-detections (hatched histogram; the numbers are multiplied by 5 for clarity). (b) Dependence of the RC extent on the HI content for all the objects in (a). The points are running averages, each one including 100 ($x < 0.2$), 59 ($x = 0.25$), 25 ($0.3 < x < 0.7$), or 8 ($x = 0.97$) measurements; the error bars are Poissonian errors on the mean.

TABLE 1
PALOMAR ROTATION CURVE DATA.

Galaxy	Other	α J2000	δ J2000	T	R_{opt} ''	R_{max} ''	V_0 km s ⁻¹	r_{PE} ''	α	Q	V_{80} km s ⁻¹	W_{80} km s ⁻¹	V_{PE} km s ⁻¹	W_{PE} km s ⁻¹
(1)	(2)	(3)	(4)	(5)	(6)	(7)	(8)	(9)	(10)	(11)	(12)	(13)	(14)	(15)
5	382-021	00 03 05.5	-01 54 51	4B	31.5	30.8	248.4	7.220	-0.0289	1	7303	420	7299±03	418±05
140	N 52	00 14 40.2	+18 34 55	3	45.1	47.8	374.0	20.576	-0.0823	1	5417	491	5414±08	535±11
144	456-044	00 15 26.8	+16 14 05	4	22.9	13.1	124.9	5.000	0.0150	0	5656	211	5640±18	259±25
400180	N 64	00 17 30.2	-06 49 29	4B	28.9	25.2	249.9	10.695	-0.0321	1	7312	398	7312±09	416±12
100184	I 1546	00 21 28.8	+22 30 24	4	23.4	22.0	172.5	6.031	0.0000	1	5820	318	5820±04	331±06
229	500-014	00 23 53.4	+28 19 57	3	16.6	24.8	117.9	4.452	0.0003	1	7235	222	7234±04	225±06
400258	M-202038	00 31 13.1	-10 28 51	4B	28.6	23.7	128.8	6.158	0.0185	1	3603	256	3614±08	274±11
400814	...	00 31 56.7	-10 15 08	4	13.5	17.4	218.5	4.730	-0.0331	1	11698	354	11701±05	359±07
351	I 34	00 35 36.5	+09 07 25	1B	48.5	45.4	317.7	6.042	-0.0036	1	5339	618	5338±07	606±10
400334	M-202082	00 40 55.0	-13 46 31	3B	24.2	26.2	112.1	1.944	0.0078	1	8459	240	8463±04	239±05
400343	N 217	00 41 33.7	-10 01 18	0	48.7	65.9	270.1	1.875	0.0000	1	3977	554	3976±10	533±14
444	519-019	00 42 04.8	+36 48 16	3	22.8	27.1	218.1	1.337	-0.0013	1	10650	430	10644±06	412±08
100917	...	00 42 11.6	+37 00 56	3	19.2	16.8	112.7	6.998	0.0350	1	10598	179	10612±08	223±10
400373	M-203006	00 45 08.8	-09 37 53	4	21.8	22.2	93.0	6.944	0.0347	1	6110	172	6112±06	193±08
400846	M-203014	00 47 25.2	-09 51 10	4	16.8	14.6	115.1	7.491	0.0300	1	5761	182	5761±06	215±08
400390	M-203015	00 47 46.2	-09 50 05	3B	34.8	38.4	197.3	3.617	0.0036	1	5767	418	5770±10	400±14
400387	UA 14	00 47 46.5	-09 53 54	3	75.1	63.1	45.8	13.587	0.0242	1	1362	98	1358±10	103±14
400848	...	00 47 51.9	-09 38 46	3	14.9	11.4	74.5	2.565	0.0103	1	6065	149	6065±07	154±10
400411	N 268	00 50 09.5	-05 11 37	5B	31.1	37.9	118.1	6.949	0.0083	1	5492	233	5494±04	238±06
534	N 280	00 52 30.2	+24 21 04	3	54.9	43.0	267.6	2.383	-0.0024	1	10185	526	10195±22	489±30
400520	N 325	00 57 47.5	-05 06 45	6	28.8	28.1	184.7	5.402	-0.0044	1	5488	344	5487±04	353±06
400522	N 329	00 58 01.3	-05 04 16	3	38.1	33.1	198.4	3.418	0.0103	1	5271	436	5267±10	435±13
400662	...	00 59 10.3	-01 53 57	3	12.8	13.2	232.2	4.202	-0.0271	1	15541	364	15546±07	386±10
641	N 353	01 02 24.5	-01 57 29	2B	21.8	21.0	174.5	4.963	-0.0099	1	4107	310	4108±08	325±11
410588	M-103075	01 02 48.0	-06 24 41	3	24.2	21.5	246.0	13.316	-0.0799	1	5775	312	5773±10	346±14
410497	384-060	01 02 48.2	-01 28 24	3	18.9	26.2	96.3	4.158	0.0565	1	5876	233	5876±05	235±07
410752	...	01 02 55.4	-06 24 42	3	13.4	9.3	200.3	1.572	0.0010	1	13604	380	13603±08	386±10
410968	...	01 03 03.7	-01 42 49	0	13991	357
410508	...	01 03 41.2	-02 20 15	3	16.0	9.1	309.8	1.922	-0.0006	1	21266	568	21266±31	576±41
410512	M-103083	01 03 56.2	-02 15 44	3	17.9	19.2	233.5	2.408	0.0120	1	15751	467	15759±04	483±05
410518	384-064	01 04 15.0	-01 06 51	3B	15.3	12.2	111.8	5.999	0.0420	1	5420	206	5409±15	224±21
410519	...	01 04 21.7	-01 31 56	4	16.9	14.5	93.1	7.143	0.0214	1	5089	137	5084±05	174±07

This figure "f5a.gif" is available in "gif" format from:

<http://arxiv.org/ps/astro-ph/0506148v1>

This figure "f5b.gif" is available in "gif" format from:

<http://arxiv.org/ps/astro-ph/0506148v1>

This figure "f5c.gif" is available in "gif" format from:

<http://arxiv.org/ps/astro-ph/0506148v1>

This figure "f5d.gif" is available in "gif" format from:

<http://arxiv.org/ps/astro-ph/0506148v1>

This figure "f5e.gif" is available in "gif" format from:

<http://arxiv.org/ps/astro-ph/0506148v1>

This figure "f5f.gif" is available in "gif" format from:

<http://arxiv.org/ps/astro-ph/0506148v1>

This figure "f5g.gif" is available in "gif" format from:

<http://arxiv.org/ps/astro-ph/0506148v1>

This figure "f5h.gif" is available in "gif" format from:

<http://arxiv.org/ps/astro-ph/0506148v1>

This figure "f5i.gif" is available in "gif" format from:

<http://arxiv.org/ps/astro-ph/0506148v1>

This figure "f5j.gif" is available in "gif" format from:

<http://arxiv.org/ps/astro-ph/0506148v1>

This figure "f5k.gif" is available in "gif" format from:

<http://arxiv.org/ps/astro-ph/0506148v1>

This figure "f5l.gif" is available in "gif" format from:

<http://arxiv.org/ps/astro-ph/0506148v1>

This figure "f5m.gif" is available in "gif" format from:

<http://arxiv.org/ps/astro-ph/0506148v1>

This figure "f5n.gif" is available in "gif" format from:

<http://arxiv.org/ps/astro-ph/0506148v1>

This figure "f5o.gif" is available in "gif" format from:

<http://arxiv.org/ps/astro-ph/0506148v1>

This figure "f5p.gif" is available in "gif" format from:

<http://arxiv.org/ps/astro-ph/0506148v1>

This figure "f5q.gif" is available in "gif" format from:

<http://arxiv.org/ps/astro-ph/0506148v1>

Table 1. Palomar Rotation Curve Data.

Galaxy	Other	α	δ	T	R_{opt}	R_{max}	V_0	r_{PE}	α	Q	V_{80}	W_{80}	V_{PE}	W_{PE}
(1)	(2)	J2000 (3)	J2000 (4)	(5)	(6)	(7)	km s ⁻¹ (8)	(9)	(10)	(11)	km s ⁻¹ (12)	km s ⁻¹ (13)	km s ⁻¹ (14)	km s ⁻¹ (15)
5	382-021	00 03 05.5	-01 54 51	4B	31.5	30.8	248.4	7.220	-0.0289	1	7303	420	7299±03	418±05
140	N 52	00 14 40.2	+18 34 55	3	45.1	47.8	374.0	20.576	-0.0823	1	5417	491	5414±08	535±11
144	456-044	00 15 26.8	+16 14 05	4	22.9	13.1	124.9	5.000	0.0150	0	5656	211	5640±18	259±25
400180	N 64	00 17 30.2	-06 49 29	4B	28.9	25.2	249.9	10.695	-0.0321	1	7312	398	7312±09	416±12
100184	I 1546	00 21 28.8	+22 30 24	4	23.4	22.0	172.5	6.031	0.0000	1	5820	318	5820±04	331±06
229	500-014	00 23 53.4	+28 19 57	3	16.6	24.8	117.9	4.452	0.0003	1	7235	222	7234±04	225±06
400258	M-202038	00 31 13.1	-10 28 51	4B	28.6	23.7	128.8	6.158	0.0185	1	3603	256	3614±08	274±11
400814	...	00 31 56.7	-10 15 08	4	13.5	17.4	218.5	4.730	-0.0331	1	11698	354	11701±05	359±07
351	I 34	00 35 36.5	+09 07 25	1B	48.5	45.4	317.7	6.042	-0.0036	1	5339	618	5338±07	606±10
400334	M-202082	00 40 55.0	-13 46 31	3B	24.2	26.2	112.1	1.944	0.0078	1	8459	240	8463±04	239±05
400343	N 217	00 41 33.7	-10 01 18	0	48.7	65.9	270.1	1.875	0.0000	1	3977	554	3976±10	533±14
444	519-019	00 42 04.8	+36 48 16	3	22.8	27.1	218.1	1.337	-0.0013	1	10650	430	10644±06	412±08
100917	...	00 42 11.6	+37 00 56	3	19.2	16.8	112.7	6.998	0.0350	1	10598	179	10612±08	223±10
400373	M-203006	00 45 08.8	-09 37 53	4	21.8	22.2	93.0	6.944	0.0347	1	6110	172	6112±06	193±08
400846	M-203014	00 47 25.2	-09 51 10	4	16.8	14.6	115.1	7.491	0.0300	1	5761	182	5761±06	215±08
400390	M-203015	00 47 46.2	-09 50 05	3B	34.8	38.4	197.3	3.617	0.0036	1	5767	418	5770±10	400±14
400387	UA 14	00 47 46.5	-09 53 54	3	75.1	63.1	45.8	13.587	0.0242	1	1362	98	1358±10	103±14
400848	...	00 47 51.9	-09 38 46	3	14.9	11.4	74.5	2.565	0.0103	1	6065	149	6065±07	154±10
400411	N 268	00 50 09.5	-05 11 37	5B	31.1	37.9	118.1	6.949	0.0083	1	5492	233	5494±04	238±06
534	N 280	00 52 30.2	+24 21 04	3	54.9	43.0	267.6	2.383	-0.0024	1	10185	526	10195±22	489±30
400520	N 325	00 57 47.5	-05 06 45	6	28.8	28.1	184.7	5.402	-0.0044	1	5488	344	5487±04	353±06
400522	N 329	00 58 01.3	-05 04 16	3	38.1	33.1	198.4	3.418	0.0103	1	5271	436	5267±10	435±13
400662	...	00 59 10.3	-01 53 57	3	12.8	13.2	232.2	4.202	-0.0271	1	15541	364	15546±07	386±10
641	N 353	01 02 24.5	-01 57 29	2B	21.8	21.0	174.5	4.963	-0.0099	1	4107	310	4108±08	325±11
410588	M-103075	01 02 48.0	-06 24 41	3	24.2	21.5	246.0	13.316	-0.0799	1	5775	312	5773±10	346±14
410497	384-060	01 02 48.2	-01 28 24	3	18.9	26.2	96.3	4.158	0.0565	1	5876	233	5876±05	235±07
410752	...	01 02 55.4	-06 24 42	3	13.4	9.3	200.3	1.572	0.0010	1	13604	380	13603±08	386±10
410968	...	01 03 03.7	-01 42 49	0	13991	357
410508	...	01 03 41.2	-02 20 15	3	16.0	9.1	309.8	1.922	-0.0006	1	21266	568	21266±31	576±41
410512	M-103083	01 03 56.2	-02 15 44	3	17.9	19.2	233.5	2.408	0.0120	1	15751	467	15759±04	483±05
410518	384-064	01 04 15.0	-01 06 51	3B	15.3	12.2	111.8	5.999	0.0420	1	5420	206	5409±15	224±21
410519	...	01 04 21.7	-01 31 56	4	16.9	14.5	93.1	7.143	0.0214	1	5089	137	5084±05	174±07
410526	...	01 04 41.5	-00 57 24	4	22.3	18.2	108.2	4.909	0.0184	1	5729	207	5734±04	228±06
410530	...	01 04 51.7	-00 38 52	3B	17.1	18.3	51.9	1.545	0.0108	0	5813	124	5809±12	114±17
410531	...	01 04 58.0	-00 50 59	0	19835	351
410534	...	01 05 26.2	-00 48 07	4	10.1	8.5	272.3	3.736	-0.0560	1	19945	369	19942±08	404±11
410541	M+004027	01 11 15.8	-00 27 21	4	16.1	22.0	74.5	4.914	0.0098	1	5323	138	5324±07	145±09
784	385-037	01 14 04.1	-01 44 33	3	22.6	37.8	128.0	1.867	0.0047	1	4916	285	4915±07	266±10
410492	FGC014a	01 14 08.1	-01 55 14	6	5008	107
410090	385-036	01 14 10.3	-01 51 14	3	17.0	8.9	75.8	4.794	0.0000	0	5094	94	5078±13	145±18
410770	A168-33	01 15 51.2	+00 08 48	3	11.9	8.6	168.4	3.500	0.0175	1	11814	312	11810±09	332±12
866	385-072	01 20 06.6	-00 12 20	7	34.4	30.0	56.1	14.556	0.0569	1	1755	84	1748±08	115±11
894	I 1681	01 21 21.2	+00 05 24	3	22.5	28.1	64.9	4.010	0.0401	1	3803	156	3806±07	156±10
111140	...	01 21 29.6	+05 17 48	3	17.0	14.1	102.5	3.191	0.0165	1	15482	197	15494±07	211±09
111144	...	01 21 29.7	+07 04 16	5	20.6	25.6	198.4	3.834	0.0230	1	23859	404	23858±08	411±11
915	N 497	01 22 23.8	-00 52 32	4B	48.5	47.7	256.0	2.517	0.0025	1	8168	534	8169±12	523±17
931	385-094	01 23 14.5	-00 42 04	3	28.5	31.7	29.3	4.938	0.0741	1	2022	76	2019±06	83±08
410148	385-093	01 23 17.0	-00 54 22	1	14.1	16.1	148.0	2.409	0.0230	1	7767	322	7765±06	326±08
410201	385-135	01 26 17.7	-01 47 37	3	13.7	10.8	169.0	4.237	0.0064	1	5575	290	5586±09	325±12

Table 1—Continued

Galaxy	Other	α J2000	δ J2000	T	R_{opt} "	R_{max} "	V_0 km s ⁻¹	r_{PE} "	α	Q	V_{80} km s ⁻¹	W_{80} km s ⁻¹	V_{PE} km s ⁻¹	W_{PE} km s ⁻¹
(1)	(2)	(3)	(4)	(5)	(6)	(7)	(8)	(9)	(10)	(11)	(12)	(13)	(14)	(15)
410468	A194-39	01 27 56.0	-01 21 29	6	14.8	11.2	39.1	2.534	0.0215	0	4657	67	4664±13	86±18
1052	N 565	01 28 10.1	-01 18 22	1	26.6	22.1	219.5	3.360	0.0046	1	4527	442	4532±20	448±28
1055	385-156	01 28 36.7	-01 43 55	1B	25.9	31.6	185.9	4.785	0.0067	1	6226	379	6231±06	376±09
1076	459-067	01 30 20.0	+17 01 17	3	21.2	26.7	295.5	3.287	-0.0016	1	12946	564	12945±05	560±07
1116	386-007	01 33 34.5	-01 05 27	6	25.4	21.8	135.0	6.515	0.0065	1	4713	213	4733±06	267±08
1120	386-010	01 34 02.4	-01 04 33	1B	27.1	49.1	213.6	5.330	-0.0318	1	4661	364	4665±07	350±09
1123	386-011	01 34 08.0	-01 01 58	2	26.9	31.9	210.1	5.865	0.0000	1	4909	415	4906±08	409±11
410269	M-305008	01 34 35.0	-15 30 13	5	27.1	40.2	253.3	21.459	-0.1073	1	5480	258	5446±04	308±06
410271	N 615	01 35 05.6	-07 20 25	2B	51.1	55.9	190.3	9.158	0.0000	1	1849	377	1848±10	377±14
410316	M-105017	01 41 07.0	-05 34 03	7B	49.8	38.1	62.3	7.962	0.0194	1	1512	132	1509±04	139±06
410955	...	01 50 54.7	-02 22 23	4	11.0	11.2	152.2	2.067	0.0000	1	14134	260	14121±08	289±11
410956	...	01 51 21.0	-02 20 48	4	11.5	15.1	104.6	2.717	0.0353	1	14489	222	14481±06	226±07
410377	M-105044	01 51 28.2	-06 30 54	7	40.3	27.1	54.3	8.271	0.0270	0	2149	108	2154±20	121±28
410490	...	01 52 41.5	-03 25 26	5	17.2	18.7	170.8	17.452	0.0000	1	5133	192	5128±05	210±07
410491	...	01 52 44.7	-03 23 55	3	13.7	13.1	72.4	4.000	-0.0120	1	5124	121	5128±08	132±11
110619	412-044	01 54 42.4	+05 25 31	3	19.2	21.5	81.4	3.667	0.0000	1	5908	155	5913±07	159±09
1428	I 1755	01 57 09.8	+14 32 59	1	29.8	27.2	257.7	4.704	0.0000	1	7937	509	7941±11	501±16
410408	N 747	01 57 30.2	-09 27 45	5	20.2	22.6	196.2	2.541	-0.0127	1	5380	362	5378±07	346±10
420050	M-106077	02 14 25.8	-07 22 06	3	50.1	58.1	176.0	10.537	-0.0076	1	5007	322	5005±06	331±09
420385	M-106078	02 14 35.9	-07 18 34	3	24.6	27.6	242.6	4.134	0.0000	1	12689	461	12685±11	464±15
420055	I 217	02 16 10.6	-11 55 31	6	54.7	51.4	107.1	23.310	0.0233	1	1902	182	1904±06	203±08
1901	N 926	02 26 06.6	-00 19 55	3B	39.5	54.8	201.0	2.610	0.0026	1	6422	434	6421±10	409±14
420126	N 958	02 30 42.4	-02 56 21	4B	5759	566
420138	M-207032	02 33 15.8	-11 44 40	6B	57.1	44.7	65.7	6.039	0.0093	1	4508	109	4491±06	141±08
2106	388-065	02 37 24.2	-01 49 18	3	19.6	20.9	139.3	3.551	0.0036	1	8609	275	8604±06	275±08
2119	N 1037	02 37 58.5	-01 50 40	3B	33.3	54.3	225.1	2.062	-0.0021	1	8534	456	8533±13	423±18
2120	388-074	02 38 07.5	+01 23 16	4B	26.4	26.7	156.5	3.623	0.0072	1	6865	314	6861±07	322±10
420173	M-307047	02 38 57.9	-14 19 13	5	27.9	35.6	90.0	5.501	0.0000	1	4566	179	4565±04	176±06
121185	...	02 38 58.4	+10 16 36	3	13.9	14.5	210.3	2.831	0.0112	1	19753	416	19756±05	413±06
2142	N 1024	02 39 11.6	+10 50 49	3	61.1	98.7	275.3	5.023	-0.0100	1	3536	508	3536±12	478±17
420612	...	02 39 18.3	-14 14 06	4	16.6	16.8	80.7	5.831	0.0397	1	9693	154	9692±07	164±09
2153	N 1030	02 39 50.5	+18 01 28	3	47.5	39.2	305.3	8.467	-0.0128	1	8574	545	8581±20	549±27
420233	N 1081	02 45 05.5	-15 35 15	3B	27.5	48.0	142.8	4.946	0.0022	1	4012	286	4009±04	284±06
420231	N 1080	02 45 09.6	-04 42 37	5B	25.6	28.6	85.0	3.890	0.0097	1	7849	172	7845±04	176±05
420242	N 1083	02 45 40.5	-15 21 25	3	33.2	27.1	196.5	7.968	0.0095	0	4079	390	4058±20	397±28
420450	M-308018	02 45 47.0	-15 30 38	3	15.7	15.3	226.7	6.321	-0.0948	1	7882	298	7883±07	309±09
420451	...	02 45 53.0	-15 33 45	3	10.0	10.2	168.2	2.811	0.0039	1	10335	307	10332±03	320±04
420405	...	02 47 00.2	-00 09 20	3	11.9	7.5	259.3	2.067	-0.0013	1	22621	464	22618±25	477±33
420434	...	02 48 34.2	-00 59 33	1	19.8	28.2	142.7	4.892	0.0196	1	7035	293	7034±05	296±07
2291	I 1856	02 48 50.7	-00 46 02	3B	27.9	31.4	179.5	2.078	0.0104	1	6487	407	6490±12	400±17
420384	389-026	02 49 35.2	-00 43 25	3	14.1	18.1	130.7	5.737	0.0164	1	6582	236	6574±07	243±10
420428	...	02 49 49.2	-00 47 35	3	15.6	16.8	233.6	2.528	-0.0045	1	13357	423	13349±08	434±10
2319	389-029	02 49 53.5	-01 00 13	5	28.8	31.4	149.5	5.476	0.0256	1	7037	310	7035±06	330±08
420308	N 1148	02 57 04.0	-07 41 08	7B	5196	260
2424	463-039	02 57 07.5	+17 30 50	4	43.2	53.4	244.6	6.353	0.0147	1	6990	535	6992±11	526±16
2479	M+008065	03 00 40.2	+00 01 13	6	35.3	38.6	92.4	13.004	0.0130	1	2850	147	2854±06	177±08
2496	FGC 653	03 02 33.4	+46 26 17	7	6796	296
121253	...	03 02 39.0	+46 27 35	3	12068	406
130457	...	03 03 45.7	+46 30 34	3	6819	277

Table 1—Continued

Galaxy	Other	α J2000 (3)	δ J2000 (4)	T (5)	R_{opt} '' (6)	R_{max} '' (7)	V_0 km s ⁻¹ (8)	r_{PE} '' (9)	α (10)	Q (11)	V_{80} km s ⁻¹ (12)	W_{80} km s ⁻¹ (13)	V_{PE} km s ⁻¹ (14)	W_{PE} km s ⁻¹ (15)
130456	...	03 03 49.2	+46 25 03	-2	7586	267
430083	N 1242	03 11 19.2	-08 54 07	6B	23.1	22.6	129.5	4.365	-0.0087	1	4008	242	4008±05	243±07
430088	N 1247	03 12 14.1	-10 28 51	5	66.6	89.3	268.4	4.144	0.0000	1	3956	549	3956±12	530±17
2628	390-041	03 16 31.7	-00 28 07	4	33.1	42.9	170.0	6.120	0.0189	1	6823	362	6821±05	365±06
430159	M-209029	03 19 17.6	-12 06 08	5	29.4	36.2	110.0	4.235	0.0199	1	4614	237	4611±02	246±03
2677	390-060	03 19 57.2	+03 35 24	3	33.5	34.6	277.5	24.155	0.0048	1	6860	332	6898±00	410±00
2703	441-009	03 22 34.4	+14 54 49	3	35.4	34.2	302.7	4.617	0.0000	1	10149	584	10148±07	585±10
430240	N 1324	03 25 01.6	-05 44 42	3	51.2	54.2	277.9	3.741	0.0037	1	5676	579	5694±09	574±13
430687	M-309037	03 25 12.1	-16 09 51	6	20.3	25.1	22.7	4.568	0.0612	0	1869	58	1866±05	57±07
2740	416-011	03 26 45.5	+07 42 50	3	37.5	35.6	247.5	4.529	-0.0017	1	7290	479	7289±06	477±08
430266	N 1337	03 28 05.8	-08 23 21	6B	129.7	85.2	92.1	14.144	0.0283	1	1257	207	1249±12	231±17
430418	I 344	03 41 29.3	-04 39 57	6B	22.4	24.2	125.0	7.794	0.0000	1	5440	226	5440±06	232±08
430428	N 1418	03 42 16.2	-04 43 55	4B	22.9	24.4	93.7	4.281	0.0171	1	4207	200	4204±06	201±08
2888	508-003	03 53 19.2	+32 19 46	4	29.1	34.7	82.2	1.611	0.0097	1	4027	195	4035±12	190±17
430621	M-311007	04 02 03.2	-16 26 49	5	7540	375
440081	FGC0471	04 16 55.4	-07 28 55	5	28.4	34.7	166.7	3.959	0.0040	1	8908	338	8905±11	333±16
23375	UA 90	04 21 13.5	-21 50 43	6	156.1	113.7	90.2	38.462	-0.0192	1	935	115	908±05	163±07
3029	393-015	04 23 58.7	-00 49 37	3	30.2	23.4	110.9	4.766	0.0095	1	5002	218	5004±12	231±17
3062	N 1586	04 30 38.2	-00 18 15	3	37.3	48.2	142.9	6.349	0.0017	1	3568	286	3570±08	284±11
440578	...	04 30 39.9	-00 17 04	-2	14.7	16.8	172.2	2.148	0.0043	1	12757	338	12756±05	340±07
3083	...	04 32 14.6	+01 43 35	5	22.4	25.5	210.0	5.580	0.0098	1	10245	411	10230±14	414±19
440522	A496-52	04 32 20.2	-13 14 09	4	8975	195
440292	N 1618	04 36 06.4	-03 08 53	4B	73.8	56.6	174.0	3.018	0.0000	1	4888	357	4890±06	342±09
440300	N 1622	04 36 36.5	-03 11 20	2	66.2	98.7	278.2	3.905	-0.0046	1	4849	533	4851±08	505±12
440614	...	04 37 09.1	-03 18 38	3	4693	124
440474	FGC495	04 37 31.2	-03 06 13	6	30.5	29.5	92.5	10.582	0.0529	1	4431	152	4430±05	198±07
440307	N 1628	04 37 35.9	-04 42 53	3	43.1	50.9	204.9	14.993	0.0150	1	3705	392	3704±09	398±12
3109	M+012059	04 37 37.7	-00 17 35	7	29.0	39.3	58.8	12.005	0.1200	1	3725	85	3703±07	137±10
440628	...	04 41 06.4	-02 51 00	0	9.2	10.8	186.6	2.212	-0.0277	1	18684	310	18686±04	306±05
23746	485 G 15	04 48 31.2	-23 55 20	3	22.7	26.0	144.1	4.346	0.0174	1	8160	300	8159±05	304±07
440373	M-213013	04 49 53.9	-10 45 14	4B	30.1	23.6	121.2	10.331	0.0301	1	4475	191	4464±12	246±16
3207	394-039	04 56 09.6	+02 09 22	3	48.9	55.2	256.2	3.668	-0.0037	1	4573	503	4572±05	480±07
440604	...	04 57 27.0	-00 04 14	5	13.7	13.9	136.3	5.666	0.0374	1	7095	254	7077±08	265±10
3214	394-051	04 57 56.7	-00 07 32	3	67.2	88.0	283.2	16.556	-0.0066	1	4914	502	4923±13	533±17
450003	M-313058	05 02 29.1	-15 32 44	5	44.0	33.7	116.8	7.770	0.0147	1	4306	200	4301±07	248±09
450233	...	05 10 51.2	-09 22 33	4	2742	27
450232	...	05 11 02.9	-09 22 29	7	16.4	12.4	32.0	5.999	0.0000	0	2607	43	2603±20	59±28
450231	...	05 12 00.5	-09 07 58	4	16.5	13.6	242.2	5.999	0.0120	1	17151	441	17150±11	443±15
3279	421-020	05 17 09.8	+06 55 37	4	37.9	35.6	317.2	13.405	-0.0094	1	8394	533	8389±13	565±17
3283	...	05 17 45.9	-01 11 13	5	33.5	37.9	159.1	14.993	0.0375	1	4526	296	4518±07	303±09
3326	347-018	05 39 37.2	+77 18 44	5	64.2	84.7	216.5	13.966	0.0102	1	4134	426	4121±11	442±15
3675	330-025	07 10 24.2	+74 53 31	5	32.7	34.6	175.1	14.388	0.0000	1	3803	282	3797±07	310±09
3757	...	07 15 07.8	+48 44 50	5	28.3	37.0	152.1	7.225	0.0217	1	5534	318	5539±05	318±07
3801	M1109046	07 21 15.3	+63 39 01	5	31.9	32.0	166.2	4.684	0.0328	0	11442	346	11412±15	391±20
3882	M+913011	07 30 43.0	+55 32 06	5	47.2	49.5	227.8	4.067	0.0000	1	11693	444	11693±07	438±10
3889	330-043	07 33 56.0	+73 38 36	2	25.2	17.8	243.7	7.310	-0.0365	0	5244	396	5242±25	405±35
3917	N 2410	07 35 02.4	+32 49 20	3	55.1	68.2	215.4	0.900	0.0005	1	4682	451	4681±06	436±09
3984	331-013	07 45 13.6	+70 01 56	3B	3885	287
4027	N 2446	07 48 39.2	+54 36 41	3	5685	431

Table 1—Continued

Galaxy	Other	α J2000 (3)	δ J2000 (4)	T (5)	R_{opt} " (6)	R_{max} " (7)	V_0 km s ⁻¹ (8)	r_{PE} " (9)	α (10)	Q (11)	V_{80} km s ⁻¹ (12)	W_{80} km s ⁻¹ (13)	V_{PE} km s ⁻¹ (14)	W_{PE} km s ⁻¹ (15)
4146	M1012054	08 01 02.0	+59 08 21	5	22.2	29.3	372.2	22.831	0.0000	1	12302	380	12346±15	445±20
4257	118-069	08 10 11.1	+24 53 32	5	40.3	63.8	81.8	8.217	0.0488	1	4138	163	4168±04	199±05
4269	088-049	08 12 01.5	+19 21 52	3	31.1	31.8	242.4	4.545	0.0000	1	8519	473	8518±10	471±14
4271	N 2523	08 15 00.4	+73 34 42	3B	68.1	49.6	189.9	11.074	-0.0026	1	3471	367	3471±12	369±17
4308	119-029	08 17 25.8	+21 41 07	5B	47.7	59.0	80.3	2.367	0.0118	1	3554	186	3566±06	197±09
180814	...	08 18 24.8	+11 37 08	3	14.0	7.5	124.1	1.952	0.0000	1	9676	223	9671±15	240±21
180815	...	08 18 27.7	+11 37 52	3	9.7	10.1	225.1	2.978	-0.0096	1	23287	370	23281±07	389±09
4370	004-005	08 22 28.7	-01 02 45	5	30.3	30.9	147.8	14.164	0.0000	1	4516	203	4496±09	257±12
4359	N 2550	08 24 33.9	+74 00 43	3	29.3	25.9	141.2	11.521	-0.0461	1	2269	213	2272±03	228±04
4392	N 2590	08 25 01.7	-00 35 32	3	43.4	41.5	219.7	2.026	0.0041	1	4990	482	5001±11	470±15
180869	...	08 27 13.3	+25 58 01	3	14.0	17.8	169.2	2.899	0.0183	1	22799	310	22781±03	340±04
4501	N 2620	08 37 28.2	+24 56 47	3	7849	592
480050	M-222023	08 38 01.2	-09 49 10	4B	22.0	23.1	181.1	6.353	-0.0381	1	4353	291	4350±05	300±07
4640	005-019	08 51 43.7	-02 08 04	5	68.7	72.5	105.5	5.804	0.0522	1	3306	298	3323±06	338±08
480077	N 2708	08 56 07.8	-03 21 37	2B	74.8	54.3	307.5	23.095	-0.0924	1	1990	406	1984±20	411±28
4691	N 2713	08 57 20.6	+02 55 14	4	81.6	87.5	339.0	3.698	-0.0048	1	3922	664	3919±13	598±18
4698	150-053	08 58 32.5	+28 15 59	2B	35.7	43.1	285.2	3.555	0.0046	1	7997	572	8001±06	581±08
26289	N 2758	09 05 31.1	-19 02 33	3	34.5	54.5	29.2	1.192	0.0558	1	1961	168	1965±06	152±08
490235	...	09 06 41.0	-10 00 30	3	23.7	41.6	133.0	3.138	0.0019	1	7612	253	7619±06	263±08
490007	M-123021	09 06 59.5	-07 23 39	4B	46.5	48.5	159.5	2.949	0.0147	1	5843	393	5834±09	380±12
490257	A754-18	09 08 03.0	-10 04 10	5	10.6	9.8	234.9	2.573	-0.0515	1	21221	348	21220±05	340±07
190812	M+422018	09 09 04.5	+20 34 52	6	22.8	21.1	20.0	11.001	0.2750	0	3001	35	2989±09	54±13
4823	N2777	09 10 41.7	+07 12 23	2	1488	92
190864	...	09 15 28.2	+11 50 05	3	8.9	5.3	50.5	1.933	0.0089	1	14715	86	14715±07	99±09
4915	006-026	09 17 29.0	-00 37 14	4	25.7	28.3	154.2	6.854	0.0000	1	4939	292	4942±04	296±06
490060	M-124007	09 17 39.2	-07 54 26	5	31.4	37.1	164.7	9.690	0.0141	1	7531	325	7521±07	323±09
4923	I 531	09 17 50.5	-00 16 44	2B	33.6	45.7	223.1	8.000	-0.0530	1	5233	347	5233±08	336±12
190809	...	09 18 33.4	+34 20 42	3	8.9	7.5	179.4	1.947	0.0065	1	13781	320	13787±07	350±09
4966	N 2841	09 22 02.0	+50 58 39	3	171.0	179.4	305.1	21.930	-0.0044	1	639	593	639±05	588±07
490302	...	09 22 09.6	-00 32 22	3	13.0	14.1	158.0	2.071	0.0083	1	16825	313	16823±05	314±06
490303	...	09 22 22.6	-00 29 18	3	16.6	14.5	252.3	2.811	-0.0253	1	26326	390	26334±07	393±09
4996	006-036	09 23 15.6	-00 43 42	4	30.5	42.1	82.1	8.818	0.1076	1	3512	211	3499±04	216±06
5010	N 2862	09 24 55.2	+26 46 29	3	49.0	69.3	306.1	16.367	-0.0090	1	4105	553	4110±13	558±18
5064	I 540	09 30 10.1	+07 54 07	3	30.3	22.9	78.1	0.463	0.0046	0	2026	204	2035±25	202±35
490096	U A 167	09 33 15.3	-16 46 04	3B	59.7	82.8	122.8	7.267	-0.0177	1	2112	238	2104±03	208±04
26543	565 G 31	09 38 00.9	-20 51 37	2	22.5	17.8	179.1	2.630	-0.0007	1	10006	345	10004±04	345±05
490155	I 562	09 46 03.7	-03 58 15	3	28.0	38.6	191.2	8.045	-0.0545	1	4793	307	4792±08	295±10
490154	...	09 46 06.4	-03 53 32	3	13.2	10.2	113.8	10.870	-0.0543	1	4842	97	4843±08	147±10
190788	092-049	09 46 30.7	+15 53 09	3	19.1	19.9	109.8	5.774	0.0058	1	3804	204	3799±05	213±07
5250	N 2998	09 48 43.5	+44 04 50	5	49.3	74.5	185.0	0.0111	1	4759	323	4804±07	402±09	
190867	...	09 49 53.4	+12 54 35	3	13.3	17.2	227.7	3.375	-0.0034	1	13978	422	13977±08	421±11
5301	M+720074	09 53 20.7	+42 50 42	5	32.7	32.2	88.6	8.361	0.0418	1	4859	177	4862±08	199±11
191021	...	09 56 06.9	+16 17 22	3	8.9	7.1	123.8	2.928	0.0088	1	21761	181	21751±06	226±08
5341	123-008	09 56 35.9	+20 38 41	5	7571	523
490308	...	10 00 28.8	-14 48 57	3	12.4	13.4	147.0	3.769	-0.0005	1	9552	259	9550±04	274±05
490200	M-226012	10 00 35.0	-14 56 54	5	27.9	51.3	171.1	3.304	-0.0095	1	9075	320	9079±06	305±08
5472	I 594	10 08 32.0	-00 40 02	2B	24.5	29.7	166.4	3.755	0.0036	1	6423	332	6422±04	333±06
500032	N 3145	10 10 09.8	-12 26 04	4B	57.2	89.1	221.0	2.313	0.0012	1	3671	466	3670±09	449±12
500383	008-082	10 14 50.0	-01 23 09	3B	14.2	14.3	60.5	3.035	0.0000	1	9421	114	9418±04	116±05

Table 1—Continued

Galaxy	Other	α J2000	δ J2000	T	R_{opt} ''	R_{max} ''	V_0 km s ⁻¹	r_{PE} ''	α	Q	V_{80} km s ⁻¹	W_{80} km s ⁻¹	V_{PE} km s ⁻¹	W_{PE} km s ⁻¹
(1)	(2)	(3)	(4)	(5)	(6)	(7)	(8)	(9)	(10)	(11)	(12)	(13)	(14)	(15)
500392	...	10 16 52.7	-01 23 05	0	10.7	6.8	195.1	0.801	-0.0021	1	19010	365	19013±10	357±13
201117	...	10 21 34.5	+23 57 34	3	18.9	30.5	156.2	8.598	-0.0695	1	6345	222	6332±06	230±08
500358	009-016	10 23 24.2	-03 23 18	3	12.2	14.0	69.1	2.596	0.0104	1	8568	135	8570±07	140±09
500075	009-018	10 23 56.4	-03 10 55	3B	43.3	43.9	476.4	36.630	-0.2930	1	5648	401	5647±16	424±22
500076	M-127007	10 24 07.4	-05 37 54	5	38.3	38.4	94.1	7.622	0.0892	1	5280	246	5278±06	266±08
500362	...	10 24 11.5	-05 37 17	4	15.8	13.9	145.0	5.179	0.0306	1	16144	250	16136±04	287±05
500324	FGC1062	10 24 17.6	-05 40 41	5	29.6	26.6	149.4	15.924	0.0000	1	5912	203	5902±07	247±10
5641	I 609	10 25 35.5	-02 12 55	3B	36.3	40.7	167.4	1.597	0.0008	1	5580	286	5548±18	335±25
500130	I 624	10 36 15.1	-08 20 02	1B	48.9	66.9	255.9	3.289	-0.0034	1	5029	509	5035±10	478±14
5787	009-091	10 38 26.2	-02 34 09	3B	36.1	48.7	195.4	7.153	0.0034	1	8276	389	8275±06	384±08
5813	184-004	10 41 08.8	+36 22 20	4	13263	425
201196	...	10 44 05.6	+26 03 41	3	9.1	6.4	100.1	2.550	0.0281	1	16144	166	16151±06	203±07
5985	I 653	10 52 06.8	-00 33 39	1	52.9	36.5	238.6	5.079	-0.0014	1	5565	463	5566±16	462±22
6340	011-059	11 19 55.2	-00 52 45	3	34.5	49.1	186.8	3.638	0.0119	1	7397	408	7400±11	406±15
510389	...	11 30 53.2	-04 21 04	5B	18.4	19.1	125.6	1.267	0.0000	1	11061	249	11062±09	242±12
510369	FGC1263	11 30 58.2	-04 05 04	5	17.2	23.4	203.3	14.577	-0.0729	1	6934	250	6935±05	252±07
510263	012-002	11 31 38.0	-03 38 51	4	17.6	19.8	194.6	4.411	0.0000	1	13729	344	13733±04	365±06
510365	...	11 32 43.0	-03 53 47	0	12.1	22.3	217.3	1.174	-0.0072	1	11847	389	11847±04	387±05
510394	...	11 33 26.0	-04 17 25	3	11.3	8.9	102.2	5.000	0.0400	1	9355	176	9348±10	194±14
211422	FGC1282	11 35 33.5	+24 57 46	6	22.0	29.6	187.9	11.173	0.0000	1	6937	311	6938±05	316±06
6595	N 3769	11 37 44.0	+47 53 34	5B	72.8	58.0	87.0	5.255	0.0087	1	746	190	741±12	195±17
6608	012-046	11 38 33.2	-01 11 04	1	21.2	30.0	156.5	3.223	-0.0046	1	6246	299	6247±06	297±08
6667	268-071	11 42 25.2	+51 35 50	5	91.2	61.9	80.5	29.155	0.0423	0	1003	127	1008±15	174±21
6720	I 728	11 44 50.4	-01 36 05	3B	36.6	33.5	183.4	3.655	-0.0014	1	8526	353	8535±08	352±10
510143	U A 245	11 45 26.1	-10 06 09	6B	49.1	53.8	121.6	30.581	-0.0483	0	1726	152	1735±12	178±17
510217	012-079	11 46 16.8	-03 10 50	5	30.3	32.7	114.3	11.001	0.0000	1	5255	200	5254±04	210±06
510383	...	11 46 33.2	-03 08 25	5	31.6	17.8	76.2	10.707	0.0000	1	5151	103	5146±10	142±14
510381	...	11 48 01.7	-03 42 25	3	18.5	12.2	126.2	2.753	0.0078	1	17427	232	17419±05	251±07
510373	...	11 49 09.6	-03 37 08	3	11.2	10.3	245.2	2.422	-0.0121	1	21205	407	21198±05	428±07
510377	...	11 49 12.6	-03 39 35	4	15.8	10.9	34.0	3.000	0.0120	1	1592	66	1594±05	72±07
6793	N 3907b	11 49 23.2	-01 05 01	3	30.0	31.4	268.2	14.815	0.0074	1	6193	427	6193±14	463±19
510161	012-097	11 49 37.9	-03 34 07	5	25.5	37.9	244.3	7.502	-0.0150	1	8149	442	8149±08	436±11
510306	012-100	11 49 49.7	-03 31 03	0	18.6	35.6	289.0	4.936	-0.0666	1	7980	423	7983±07	412±09
6815	N 3917	11 50 45.5	+51 49 28	5	113.7	130.5	111.5	27.027	0.0392	1	929	162	973±07	255±10
6869	N 3949	11 53 41.7	+47 51 28	5	53.4	61.0	140.2	11.074	-0.0198	1	807	255	808±07	251±10
510177	I 2974	11 53 49.4	-05 10 01	5	52.1	77.3	216.0	5.200	0.0095	1	5740	466	5742±08	464±12
6928	N 3987	11 57 20.8	+25 11 42	3	54.7	50.5	185.1	39.683	0.3968	0	4604	240	4540±35	422±49
6973	I 750	11 58 51.9	+42 43 20	3	722	318
211853	...	11 59 50.9	+08 47 35	0	8.3	10.8	68.7	2.000	0.0000	1	10542	126	10535±06	131±08
7015	N 4043	12 02 23.0	+04 19 47	3	6438	150
510212	M-131002	12 02 26.0	-04 18 28	5	32.9	33.6	153.8	11.001	0.0110	1	5738	275	5741±08	296±10
520002	N 4050	12 02 53.7	-16 22 23	2B	86.7	67.0	189.6	35.336	0.0000	1	1790	301	1777±17	345±24
7067	N 4079	12 04 49.7	-02 22 54	3	34.3	33.3	215.5	4.914	-0.0058	1	6076	395	6076±09	405±13
520006	M-231017	12 06 51.0	-11 05 39	6	51.8	54.2	334.4	33.445	-0.1672	1	4460	369	4459±06	384±09
520011	N 4129	12 08 53.2	-09 02 11	6	42.2	66.1	125.9	15.873	-0.0157	1	1191	227	1196±05	224±07
7196	098-095	12 11 59.2	+15 24 03	3	29.9	30.0	680.1	26.738	-0.3209	1	7098	568	7105±08	573±11
221736	...	12 15 49.2	+13 11 48	3	9.8	9.2	183.8	2.884	0.0202	1	19452	303	19465±07	357±09
221829	...	12 16 03.2	+14 00 46	4	11.4	11.1	113.7	4.623	0.0370	1	15256	190	15251±04	216±05
221828	FGC1395	12 16 11.6	+13 59 34	6	18.7	17.4	94.1	5.956	0.0476	1	7687	175	7679±05	202±07

Table 1—Continued

Galaxy	Other	α J2000 (3)	δ J2000 (4)	T (5)	R_{opt} '' (6)	R_{max} '' (7)	V_0 km s ⁻¹ (8)	r_{PE} '' (9)	α (10)	Q (11)	V_{80} km s ⁻¹ (12)	W_{80} km s ⁻¹ (13)	V_{PE} km s ⁻¹ (14)	W_{PE} km s ⁻¹ (15)
7297	N 4226	12 16 26.2	+47 01 32	3	23.4	19.7	242.1	3.704	0.0000	1	7253	457	7261±10	472±13
7337	013-121	12 18 08.6	-01 03 52	4	25.2	44.9	175.5	6.254	-0.0405	1	5727	288	5729±07	283±10
221991	...	12 19 44.0	+29 34 49	3	10.2	11.3	184.5	2.269	-0.0068	1	19385	325	19384±05	332±07
7478	N 4357	12 23 58.7	+48 46 45	3	64.8	54.8	248.5	10.741	-0.0301	1	4158	411	4154±07	400±10
221659	...	12 25 41.7	+07 10 01	3	9.8	16.1	127.2	2.464	0.0111	1	7153	256	7141±05	255±07
221928	...	12 26 51.7	+31 05 39	3	18.5	15.0	264.2	1.146	-0.0011	1	17951	507	17946±10	489±13
222003	...	12 27 06.5	+06 25 32	3	13.3	12.2	163.1	3.264	0.0000	1	7596	295	7596±04	313±06
520062	N 4428	12 27 28.6	-08 10 05	3	42.7	37.4	145.6	4.686	0.0048	1	2975	305	2978±07	301±10
520063	N 4433	12 27 38.7	-08 16 48	3B	34.6	52.7	173.1	8.873	0.0088	1	2993	352	2997±06	347±09
221950	...	12 32 59.7	+03 23 37	3	9.7	13.7	127.6	1.890	0.0284	1	13252	279	13260±04	278±05
520104	M-132035	12 40 15.8	-09 17 54	4B	26.6	28.1	146.5	3.724	0.0149	1	6354	310	6351±04	317±06
7844	...	12 40 49.7	+73 43 08	5	1835	111
7883	015-002	12 42 57.2	-01 13 46	5	60.0	55.6	138.8	15.432	0.0191	1	3200	267	3204±04	289±06
520620	015-003	12 43 02.9	-01 16 58	5	19.4	18.5	123.5	4.292	-0.0129	1	7123	225	7122±05	225±07
7893	N 4642	12 43 17.6	-00 38 41	3	40.8	52.0	133.7	10.593	0.0216	1	2664	260	2672±10	281±14
520135	N 4658	12 44 37.7	-10 05 00	2B	2391	229
520136	N 4663	12 44 47.0	-10 11 52	-2	20.6	11.2	129.1	1.500	0.0000	0	2401	275	2387±35	256±49
520563	...	12 44 52.0	-00 25 48	3	16.3	17.1	325.8	4.085	-0.0378	1	24647	487	24661±08	502±11
7931	N 4668	12 45 31.7	-00 32 09	5B	32.0	43.6	49.8	12.005	0.0720	1	1630	97	1636±07	110±10
7963	015-022	12 47 52.7	-01 11 10	5	27.1	37.9	121.6	5.271	0.0374	1	7037	296	7041±05	282±07
520234	N 4781	12 54 23.2	-10 32 09	6B	72.5	90.4	80.3	8.554	0.0428	1	1270	216	1267±06	218±08
520284	M-233068	12 57 05.6	-12 16 20	6B	49.1	64.5	223.6	1.330	-0.0001	1	6350	449	6344±07	436±09
8067	015-044	12 57 12.0	-01 42 24	3	44.9	55.1	114.7	8.313	0.0166	1	2836	248	2833±05	247±07
222035	...	12 59 44.2	+14 10 54	3	14165	194
520403	M-133072	13 01 55.2	-06 55 34	6	59.9	52.7	190.3	25.189	-0.0756	1	3595	255	3593±06	280±08
530038	N 4995	13 09 40.5	-07 50 00	4	60.8	51.0	131.7	4.283	0.0021	1	1741	269	1742±07	270±10
8238	016-013	13 09 41.0	-01 02 53	5	25.8	39.2	136.4	2.701	0.0162	1	7338	308	7331±06	307±09
530628	...	13 09 42.0	-07 53 08	3	20.0	23.4	122.7	5.817	0.0349	1	6742	245	6744±04	260±05
530046	M-134010	13 10 28.2	-07 38 59	3	18.4	21.1	156.6	4.859	-0.0157	1	6887	280	6880±03	281±05
530631	...	13 16 34.0	-02 17 22	3	12.6	12.7	53.3	5.000	0.0400	1	4009	102	4008±04	106±06
8348	I 4218	13 17 03.4	-02 15 40	3	25.2	31.8	178.2	5.244	0.0105	1	5792	367	5794±05	364±06
530085	M-334041	13 17 06.0	-16 15 07	5	50.4	55.3	112.4	15.106	0.0452	1	2651	232	2651±04	247±06
530090	I 4221	13 18 30.2	-14 36 28	5	35.6	34.7	100.8	7.981	0.0319	1	2892	213	2889±03	226±04
530603	...	13 18 56.2	-14 54 13	3	19.4	12.6	242.9	1.500	-0.0045	1	10740	461	10739±12	442±16
530097	N 5073	13 19 20.6	-14 50 37	3	67.2	83.9	160.4	11.074	0.0111	1	2761	343	2761±08	338±11
530104	N 5079	13 19 38.0	-12 41 56	3B	45.9	29.3	96.2	5.470	0.0092	1	2238	194	2242±08	206±11
530112	N 5088	13 20 20.2	-12 34 14	6B	50.4	68.7	81.5	12.165	0.0897	1	1449	210	1449±05	219±07
29608	N 5134	13 25 18.2	-21 08 06	3	74.3	55.7	40.6	3.720	0.0186	1	1774	118	1773±15	111±21
530226	M-234055	13 28 20.2	-11 46 59	5	32.1	52.9	114.9	8.889	0.0844	1	6012	299	6006±09	286±12
8475	N 5174	13 29 25.7	+11 00 28	5	61.6	70.7	292.4	10.246	-0.0154	1	6838	533	6838±09	518±12
8485	N 5183	13 30 06.1	-01 43 13	3	4313	360
8487	N 5184	13 30 11.5	-01 39 47	3	39.3	56.5	177.9	6.024	0.0024	1	3989	356	3991±08	356±11
530277	M-234061	13 31 04.0	-15 06 03	5	35.6	43.3	99.5	7.215	-0.0002	1	4218	200	4217±03	195±04
8518	N 5207	13 32 14.0	+13 53 31	3	32.8	53.9	245.2	1.673	0.0000	1	7650	506	7651±06	478±09
530511	M-335003	13 33 12.3	-16 08 21	3	17.3	18.6	59.8	2.758	-0.0138	1	6245	115	6248±04	107±06
530316	M-335004	13 33 13.8	-16 07 08	2B	55.4	61.3	257.9	0.990	0.0040	1	6140	614	6133±12	617±17
231092	045-042	13 36 35.5	+08 11 34	3	16.9	20.1	161.7	7.812	0.0000	1	6958	250	6968±04	280±06
231195	...	13 45 36.9	+22 03 16	5	14.1	13.8	110.8	3.075	0.0031	1	7974	205	7971±06	217±08
8766	I 944	13 51 30.8	+14 05 30	1	42.6	41.0	307.5	6.427	-0.0017	1	6995	571	6997±03	594±04

Table 1—Continued

Galaxy	Other	α J2000 (3)	δ J2000 (4)	T (5)	R_{opt} '' (6)	R_{max} '' (7)	V_0 km s ⁻¹ (8)	r_{PE} '' (9)	α (10)	Q (11)	V_{80} km s ⁻¹ (12)	W_{80} km s ⁻¹ (13)	V_{PE} km s ⁻¹ (14)	W_{PE} km s ⁻¹ (15)
231174	...	13 52 21.2	+38 11 43	3	13.9	7.0	135.8	1.075	0.0000	1	5658	264	5660±20	267±28
231135	...	13 53 27.2	+20 56 59	3	10.7	9.9	305.0	9.124	-0.1825	1	8495	275	8484±09	322±12
8828	132-040	13 54 26.7	+21 49 45	4	31.5	21.1	236.3	6.761	-0.0005	1	8284	373	8302±28	454±39
8831	N 5356	13 54 58.4	+05 20 00	3	74.9	65.4	139.5	19.305	0.0116	1	1394	263	1390±06	284±08
8844	018-004	13 55 59.4	-01 15 42	5B	31.5	45.9	156.2	4.606	-0.0046	1	7405	299	7406±06	295±08
8918	074-031	14 00 14.5	+08 58 01	3	4136	262
230925	074-035	14 00 31.0	+08 39 01	5	4548	143
8927	046-035	14 01 10.5	+07 28 55	4	7116	263
540004	N 5426	14 03 25.0	-06 04 09	4B	59.0	51.8	154.7	3.466	-0.0002	1	2574	315	2572±05	306±07
8994	018-042	14 04 52.5	-00 36 39	4B	27.0	26.0	141.2	4.794	-0.0048	1	7432	269	7435±07	267±10
9013	N 5474	14 05 01.3	+53 39 44	6	283	17
9039	M1213030	14 06 56.4	+72 07 20	5	28.2	38.6	333.7	11.364	-0.0428	1	10081	530	10079±08	529±11
9079	N 5496	14 11 37.7	-01 09 28	5	144.2	103.0	110.2	26.385	0.0000	1	1573	183	1560±08	218±11
241267	M+631092	14 17 11.6	+35 24 30	3	16.1	19.0	259.6	2.753	-0.0248	1	12827	445	12823±07	424±09
241334	M+632004	14 21 08.1	+35 17 45	5	20.3	24.8	57.0	8.834	0.0177	1	3651	89	3661±04	105±05
540075	019-007	14 21 55.2	-00 33 24	0	12.2	12.4	228.6	2.685	-0.0186	1	15685	393	15683±04	393±05
9201	N 5584	14 22 23.7	-00 23 18	5	88.8	75.8	86.9	21.142	0.0155	1	1652	162	1661±07	181±09
241270	M+632024	14 24 12.0	+35 08 45	3	15.0	15.0	154.1	3.030	0.0091	1	8564	301	8567±03	311±04
9231	N 5616	14 24 20.7	+36 27 39	4	45.0	44.9	208.6	6.046	0.0300	1	8427	513	8424±16	496±22
540084	N 5604	14 24 42.5	-03 12 44	1	35.8	47.6	143.6	3.537	0.0059	1	2758	302	2760±05	302±07
241336	...	14 24 58.2	+35 21 15	3	17.0	20.6	90.7	5.120	0.1024	1	8639	218	8642±03	228±04
540242	019-024	14 25 49.7	-02 20 01	3	16142	424
9250	N 5618	14 27 11.8	-02 15 46	5B	41.7	41.4	129.6	4.673	0.0047	1	7135	260	7132±07	264±10
540107	M-237006	14 32 52.7	-12 58 30	4B	41.4	43.0	107.5	12.300	-0.0123	1	4148	180	4140±03	196±03
9462	N 5719	14 40 56.0	-00 19 04	3	60.3	57.7	180.8	2.106	-0.0026	1	1733	355	1733±03	332±05
540121	N 5728	14 42 23.7	-17 15 06	1B	89.2	61.0	164.3	0.615	-0.0002	0	2804	350	2804±20	317±28
9483	I 1048	14 42 57.9	+04 53 24	3	50.8	90.0	186.7	23.202	-0.0580	1	1638	273	1632±07	288±09
9512	N 5750	14 46 11.1	-00 13 22	1B	55.6	51.4	191.1	6.645	0.0000	1	1692	354	1696±13	380±18
540233	...	14 47 03.5	-13 48 41	3	10.3	10.6	121.2	3.208	0.0321	1	12969	217	12963±03	246±04
540133	I 1055	14 47 25.5	-13 42 58	3	49.0	56.6	171.6	5.889	0.0177	1	2905	380	2899±06	390±08
540235	...	14 47 39.2	-13 38 13	6	15.6	19.2	19.2	9.709	1.1553	1	2411	77	2408±05	87±07
540136	M-238015	14 47 55.9	-14 16 56	6B	54.4	64.6	97.4	12.531	0.0000	1	2057	163	2056±09	191±12
9537	193-001	14 48 26.7	+34 59 50	3	59.8	67.9	274.5	3.368	-0.0051	1	8820	544	8822±14	485±19
9538	I 1058	14 49 12.3	+17 01 13	2	33.4	25.0	164.0	2.039	0.0510	1	11212	486	11220±16	580±22
241306	...	14 51 18.7	+16 41 41	5	10.7	7.5	83.6	3.000	0.0120	1	13828	155	13842±11	162±15
9579	N 5775	14 53 57.4	+03 32 39	5	85.0	92.8	99.7	8.285	0.1011	1	1711	345	1695±08	404±11
9631	N 5792	14 58 22.7	-01 05 28	3B	1907	429
9645	N 5806	15 00 00.3	+01 53 28	3	66.5	77.5	148.9	1.018	0.0010	1	1360	308	1364±15	316±21
9681	M+731023	15 03 39.7	+42 07 33	5	27.3	28.1	105.2	8.969	0.0386	1	5181	196	5174±10	220±14
550006	M-238032	15 04 27.1	-14 26 23	6	2922	165
550017	N 5861	15 09 16.2	-11 19 20	5B	67.6	64.2	109.4	5.807	0.0313	1	1876	279	1875±05	297±07
9805	N 5908	15 16 43.0	+55 24 31	3	58.1	65.7	329.6	8.410	-0.0083	1	3308	618	3307±06	614±08
9818	N 5913	15 20 55.4	-02 34 40	3B	53.2	30.6	160.3	11.669	0.0154	0	1996	314	1988±27	337±38
550063	M-139005	15 23 20.0	-04 09 06	2B	36.8	29.7	190.9	30.303	-0.2424	1	2012	163	2009±06	188±08
9888	I 1125	15 33 05.6	-01 37 42	3	31.0	42.6	90.1	5.350	0.0187	1	2813	194	2805±08	197±11
9969	N 5985	15 39 36.7	+59 19 52	3B	99.7	90.3	242.2	7.168	0.0072	1	2531	523	2520±09	528±12
31301	583 G 7	15 49 54.2	-21 02 58	4	33.2	40.8	324.2	10.449	-0.0627	1	7307	480	7299±06	486±09
550113	022-042	15 50 02.0	-02 49 28	5	43.7	52.5	204.2	4.335	0.0000	1	8341	400	8338±08	397±11
10230	N 6070	16 09 58.5	+00 42 32	5	92.6	73.6	176.6	12.376	0.0019	1	2019	344	2018±14	355±20

Table 1—Continued

Galaxy	Other	α	δ	T	R_{opt}	R_{max}	V_0	r_{PE}	α	Q	V_{80}	W_{80}	V_{PE}	W_{PE}
(1)	(2)	J2000	J2000	(5)	"	"	km s ⁻¹	"	(10)	(11)	km s ⁻¹	km s ⁻¹	km s ⁻¹	km s ⁻¹
		(3)	(4)		(6)	(7)	(8)	(9)			(12)	(13)	(14)	(15)
10306	023-031	16 16 43.5	+00 14 46	3	48.0	52.9	293.2	6.684	-0.0086	1	9179	539	9179±08	533±11
10478	M1120021	16 35 44.0	+68 25 40	4	33.0	43.1	185.9	6.418	0.0128	1	7640	373	7631±07	384±10
10554	025-006	16 48 21.2	-01 37 09	5	1564	147
10641	M1024079	16 58 06.4	+58 53 08	5	32.5	31.7	111.5	9.001	0.0090	1	5262	219	5241±19	220±26
10681	252-018	17 03 32.7	+45 27 33	5	33.3	32.2	247.6	7.530	0.0000	1	9843	450	9847±06	474±08
10692	139-034	17 05 28.0	+23 09 11	3	37.1	55.5	312.7	8.897	-0.0445	1	9328	507	9332±08	486±11
10706	197-035	17 06 28.3	+38 21 47	4	8232	375
10816	252-042	17 19 18.7	+49 57 42	5	9954	576
11102	...	18 02 58.2	+52 06 51	4	21.0	33.7	186.2	8.000	-0.0160	1	14528	325	14528±09	316±12
11268	201-006	18 32 06.9	+37 36 48	4	26.8	24.8	201.8	6.532	-0.0056	1	7898	366	7894±07	378±09
11300	N 6689	18 34 50.0	+70 31 26	5	108.0	132.9	70.8	12.531	0.0302	1	506	161	483±25	178±35
11429	N 6792	19 20 57.4	+43 07 56	3B	59.8	54.7	258.7	7.353	-0.0074	1	4641	485	4641±17	479±23
11527	372-016	20 13 54.5	-01 09 27	3	32.9	44.9	221.8	6.743	0.0000	1	5487	446	5486±06	432±08
33419	596 G 36	20 25 50.0	-18 31 24	5	21.8	24.1	122.1	4.801	0.0000	1	6959	216	6970±06	236±08
33506	528 G 11	20 30 13.1	-23 02 09	5	54.3	33.9	104.4	24.096	0.0407	0	6095	153	6097±02	200±03
33670	597 G 20	20 39 07.0	-20 14 25	4	28.9	31.5	211.3	3.505	0.0078	1	8415	440	8417±06	437±08
600185	K2045-17	20 48 38.4	-17 14 29	6	8382	274
600138	M-153012	20 49 52.0	-07 01 17	5	43.5	79.1	228.3	15.152	0.0168	1	6031	454	6047±07	443±10
11649	374-028	20 55 27.6	-01 13 31	1B	40.4	53.4	130.3	2.041	0.0000	1	3807	269	3807±07	257±09
11651	470-006	20 57 15.3	+25 58 06	7	1542	217
310030	426-015	21 12 01.2	+11 29 45	1	20.6	16.5	105.2	2.017	0.0057	1	5034	221	5033±10	219±13
610024	375-011	21 13 12.8	-00 21 58	5	20.7	26.1	118.0	3.917	0.0196	1	6135	241	6136±04	254±06
11712	N 7047	21 16 27.6	-00 49 36	3	33.4	27.7	199.7	7.062	-0.0002	1	5815	386	5811±10	388±14
610044	M-254005	21 20 23.2	-13 10 16	5	26.2	28.1	237.9	4.073	0.0204	1	9005	532	9008±13	522±17
310173	I 1398	21 46 11.6	+09 33 48	3	13.9	21.5	130.6	2.141	0.0227	1	8406	290	8408±05	291±07
610495	...	21 56 49.5	-07 45 33	3	9.8	5.1	155.2	2.235	0.0000	0	16515	239	16506±11	291±15
610499	...	21 58 05.8	-07 50 43	3	23.8	26.7	226.4	17.730	-0.1773	1	5287	234	5282±07	250±09
610147	I 1417	22 00 21.5	-13 08 49	3	26.1	49.1	250.1	5.956	-0.0241	1	5391	433	5390±05	433±07
34992	532 G 15	22 03 08.1	-22 23 40	6	25.1	25.5	36.3	14.881	0.0893	1	1747	60	1746±08	68±11
11893	M+648005	22 04 06.8	+35 56 18	5	49.5	61.8	377.1	37.453	0.0000	1	5578	544	5574±10	543±14
620012	M-156002	22 09 34.4	-06 06 51	6B	37.6	47.1	123.8	5.872	0.0000	1	5036	245	5036±08	243±10
620036	M-357001	22 20 12.8	-15 56 52	3B	33.6	38.4	134.2	5.495	0.0165	1	5070	292	5067±05	290±06
620093	M-357018	22 31 55.5	-17 08 43	5B	37.4	31.7	95.9	8.130	0.0207	1	5524	170	5543±09	204±12
12113	N 7331	22 37 04.0	+34 24 58	3	179.8	275.2	265.4	23.753	-0.0117	1	874	420	828±25	482±35
620266	...	22 39 12.5	-02 26 19	3	16.5	13.1	111.7	4.000	0.0124	1	15686	201	15689±06	220±08
620160	N 7344	22 39 36.0	-04 09 31	2B	29.6	29.4	197.1	1.360	-0.0009	1	7441	394	7444±06	377±08
12174	N 7364	22 44 24.2	-00 09 44	1	40.0	37.0	215.8	2.565	-0.0077	1	4867	402	4865±05	374±08
620180	N 7378	22 47 47.5	-11 48 59	2B	35.5	26.8	94.2	7.087	0.0149	1	2577	180	2578±06	199±08
320484	453-037	22 58 57.2	+20 23 29	2	19.4	14.5	218.1	6.227	-0.0187	1	7141	330	7133±09	383±12
12294	N 7448	23 00 03.7	+15 58 48	5	46.7	57.1	125.0	5.963	0.0060	1	2216	269	2205±20	260±28
12316	N 7463	23 01 52.0	+15 58 53	3	2379	199
12348	379-029	23 05 18.7	+00 11 21	1	7609	359
12363	379-034	23 06 31.5	+00 10 18	3	26.4	33.3	76.4	1.060	0.0159	1	7464	217	7472±11	208±14
630018	M-158022	23 07 25.5	-05 09 27	6	7400	339
630079	M-259004	23 10 21.7	-08 41 20	5B	42.3	48.2	531.2	61.350	-0.1227	1	7094	454	7097±12	473±17
12453	N 7547	23 15 03.4	+18 58 23	1B	29.9	18.3	170.2	2.000	0.0040	0	5080	374	5088±35	355±49
35971	604 G 7	23 15 17.2	-21 21 57	3	7703	413
12457	N 7549	23 15 17.2	+19 02 28	3B	4714	343
12484	N 7587	23 17 59.2	+09 40 48	1	32.3	38.6	254.3	2.201	0.0088	1	8763	573	8762±10	558±14

Table 1—Continued

Galaxy	Other	α J2000	δ J2000	T	R_{opt} ''	R_{max} ''	V_0 km s ⁻¹	r_{PE} ''	α	Q	V_{80} km s ⁻¹	W_{80} km s ⁻¹	V_{PE} km s ⁻¹	W_{PE} km s ⁻¹
(1)	(2)	(3)	(4)	(5)	(6)	(7)	(8)	(9)	(10)	(11)	(12)	(13)	(14)	(15)
12506	454-039	23 19 30.5	+16 04 27	5	40.0	42.9	142.9	6.075	0.0275	1	7218	339	7225±14	329±19
330252	454-044	23 20 37.2	+16 12 33	2	7039	315
12556	N 7641	23 22 30.7	+11 53 32	1	37.7	51.4	428.6	28.169	-0.0845	1	7865	515	7866±13	547±17
12591	497-015	23 25 21.8	+28 29 39	0	6935	923
12641	454-077	23 30 54.5	+20 15 02	4	31.4	32.7	66.6	6.192	0.0619	1	2707	157	2713±04	172±06
630209	M-160005	23 33 44.0	-03 04 52	7B	33.6	37.4	80.5	13.004	0.0650	1	5216	156	5225±09	171±13
630213	N 7700	23 34 30.1	-02 57 14	-2	31.9	45.8	242.6	7.305	-0.0296	1	5250	412	5246±14	410±19
630216	I 5334	23 34 36.2	-04 32 02	3	39.5	40.1	109.8	1.885	0.0161	1	2221	274	2218±06	291±08
12825	...	23 53 13.3	+10 53 40	4	27.0	29.3	356.0	13.158	-0.0211	1	21465	514	21461±09	554±11
12834	N 7782	23 53 54.0	+07 58 14	3	52.5	52.4	262.4	2.933	0.0029	1	5399	554	5399±10	543±13
630350	I 1524	23 59 05.6	-04 07 34	3	29.4	32.4	188.6	2.220	-0.0044	1	5756	370	5744±07	349±10